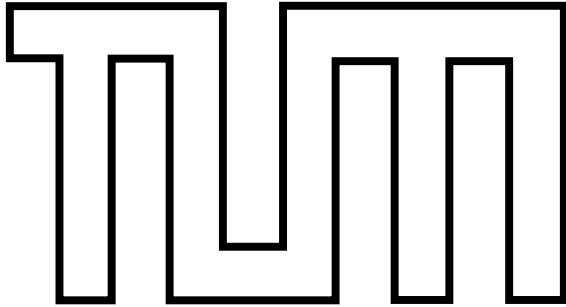


LUDWIG MAXIMILIANS UNIVERSITY &
TECHNICAL UNIVERSITY OF MUNICH



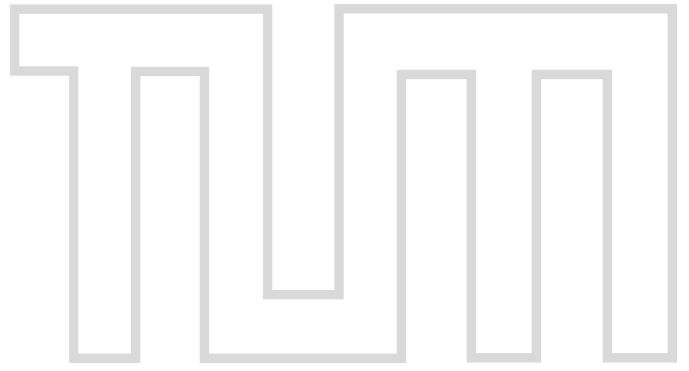
Dynamical Properties of the J_1 - J_2 Heisenberg Model on the Triangular Lattice

Ester Pagès Fontanella

supervised by Prof. Jan von Delft,
Department of Physics,
Ludwig Maximilian University of Munich

A thesis submitted for the degree of
M.Sc. Quantum Science & Technology

©2025 – ESTER PAGÈS FONTANELLA
All rights reserved.



Dynamical Properties of the J_1 - J_2 Heisenberg Model on the Triangular Lattice

Ester Pagès Fontanella

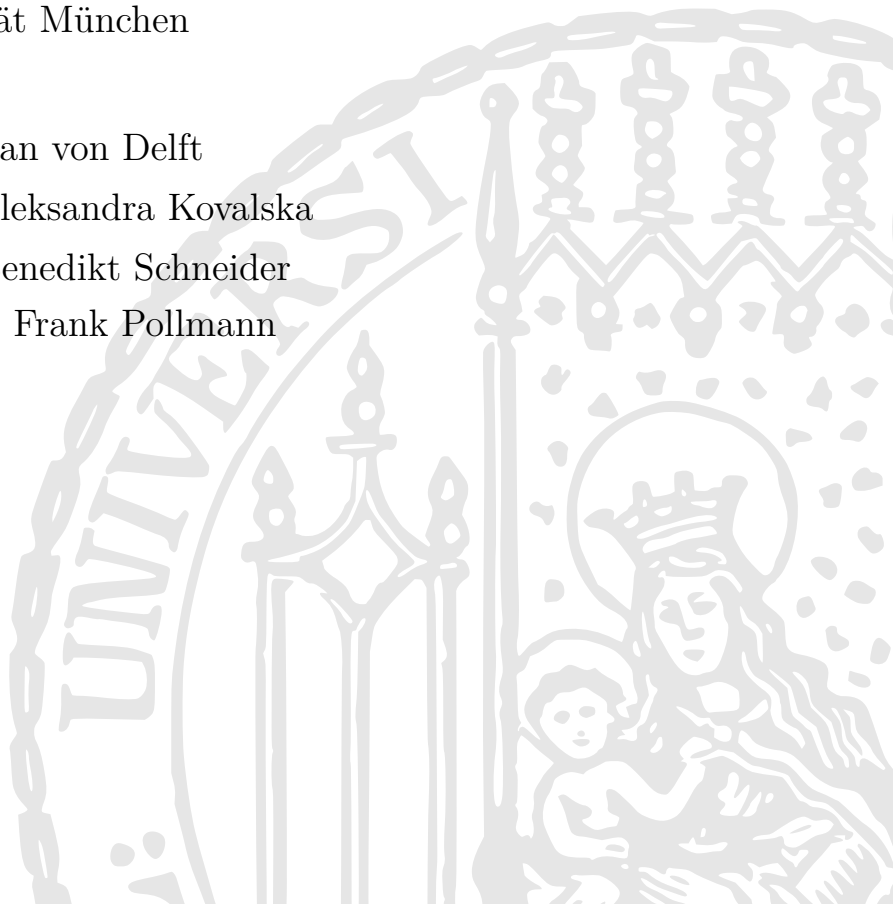
M.Sc. Quantum Science & Technology,
Ludwig-Maximilians-Universität München,
Technische Universität München

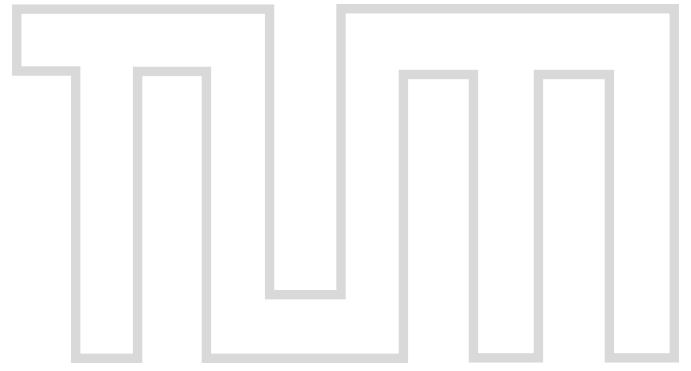
Supervisor: Prof. Jan von Delft

Co-Supervisors: Oleksandra Kovalska
Benedikt Schneider

Second Examiner: Frank Pollmann

July 31, 2025, Munich





Dynamische Eigenschaften des J_1 - J_2 Heisenberg-Modells in einem dreieckigen Gitter

Ester Pagès Fontanella

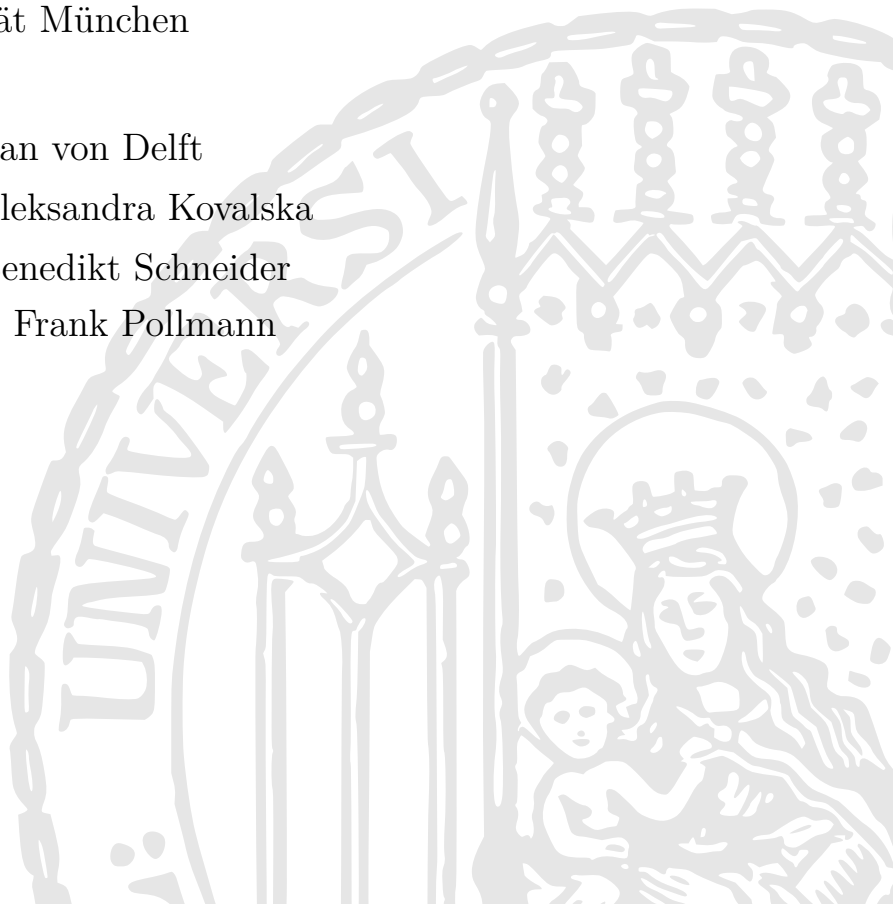
M.Sc. Quantum Science & Technology,
Ludwig-Maximilians-Universität München,
Technische Universität München

Supervisor: Prof. Jan von Delft

Co-Supervisors: Oleksandra Kovalska
Benedikt Schneider

Second Examiner: Frank Pollmann

July 31, 2025, Munich



Dynamical Properties of the J_1 – J_2 Heisenberg model

ABSTRACT

The precise nature of the quantum spin liquid (QSL) candidate region in the spin- $\frac{1}{2}$ triangular lattice Heisenberg antiferromagnet (TLHAF) remains an open and actively debated question in condensed matter physics. In this thesis, we investigate static and dynamical properties of the J_1 – J_2 TLHAF model on a finite YC6-0-36 cylinder, fixing $J_1 = 1$ and focusing on three representative regimes: the 120° Néel ordered phase at $J_2 = 0$, the QSL candidate region at $J_2 = 0.125$, and the stripe ordered phase at $J_2 = 0.2$. Ground states are obtained using the controlled bond expansion density matrix renormalization group (CBE-DMRG) method, and real-frequency spectral functions are computed via the novel tangent space Krylov (TaSK) method.

Our results reproduce the known features of the ordered phases and provide evidence of suppressed magnetic order and broadened spectral features at the point $J_2 = 0.125$, consistent with QSL behavior. In particular, the dynamical spin structure factor at $J_2 = 0.125$ reveals gapped excitations and a broad continuum at high energies, suggesting the presence of fractionalized excitations. However, finite-size effects and numerical limitations prevent a conclusive identification of the QSL type. In the stripe-ordered phase, sharp spectral features and roton-like minima at characteristic momenta are recovered. Together, these findings serve as non-trivial benchmark of the TaSK scheme in ordered regimes, and demonstrate its ability to probe the dynamical properties of challenging exotic phases of matter.

Acknowledgements

Firstly, I would like to thank Prof. Jan von Delft for giving me the opportunity to work in this project, for his unwavering support, and for welcoming me into the research group. It has been a pleasure and a privilege to work with you and learn from you. Thank your passion for driving physics further and for showing me the captivating world of tensor networks.

Secondly, I would like to express my deepest gratitude to Sasha (O. Kovalska) for her endless support — both academic and personal — during this whole process. This project wouldn't have been possible without you. Benedikt, who has always been open to discussions and offered his steady support. Both of them brought light when I was lost in my lattice.

A heartfelt thank you to Hong-Hao, who always provided me with new insights, professionally and personally. Thanks also to Andreas, who was always available for fruitful scientific discussions. I have learnt a lot during this process, and I would like to thank the whole group for always being ready to jump into any discussion and for keeping a bright mood in the group. Special thanks to Ming and Felipe, always up for a QSpace consultation, and Gianluca, who greatly contributed to the camaraderie in the office.

I also want to thank my friends, especially Francesc, Guille, Jady, Klaudia, Kyrana, Marc, Núria, and Sali, who were always there for the ups and downs, always ready to hear me talking about my thesis, and who made some of the most stressful moments much easier to navigate. To my flatmates, Alex and Chris, who have been like my siblings this past year and have made me feel at home in Munich.

Special thanks to those friends who, despite the distance that separates us, have been constantly supporting me. Especially Ana, Marina and Berta, who I carry with me wherever I go.

Lastly, but by no means least, I want to thank my family. They have always given me the wings to fly and the freedom to find my own path, always supporting me every step of the way.

Contents

Contents	5
Introduction	1
1 Method	3
1.1 Tensor Networks - formalism	3
1.2 Density Matrix Renormalization Group	9
1.3 Tangent space Krylov (TaSK) scheme	11
2 Theoretical Background	15
2.1 J_1 – J_2 Triangular Lattice Antiferromagnetic Heisenberg Model .	15
2.2 Candidate Spin Liquid Phases	16
3 Results	19
3.1 Preliminary considerations	19
3.2 Physical Observables: Definitions	22
3.3 YC6–0–36 geometry	26
4 Summary and outlook	33
A Complementary Plots for the YC6–0–36 geometry	35
B YC6-2-36 geometry	37
Bibliography	39

Introduction

Many-body quantum systems exhibit a rich variety of collective phenomena that continue to inspire both theoretical and experimental research. Among them, magnetic materials with interacting spins have long served as a central platform for exploring fundamental questions about quantum correlations and emergent phases. Understanding how such systems behave — particularly when the interactions are strong and the geometry of the lattice induces frustration — is a key challenge in modern condensed matter physics.

Frustrated quantum magnets, in particular, offer fertile ground for discovering unconventional states of matter. One notable example are quantum spin liquids, e.g Dirac or Kitaev QSLs: highly entangled phases that lack any form of conventional symmetry-breaking order, even at zero temperature [1]. A paradigmatic setting for studying such phenomena is the triangular lattice Heisenberg antiferromagnet (TLHAF), where localized spins interact via exchange couplings. In this work, we consider the J_1 - J_2 TLHAF, where J_1 and J_2 correspond to nearest-neighbor and next-nearest neighbor interactions, respectively.

When only nearest-neighbor interactions are present, the system exhibits long-range 120° magnetic order in its ground state [2–4]. However, the addition of next-nearest-neighbor couplings increases geometric frustration and can destabilize this order [5, 6]. For sufficiently large J_2 , the system develops a collinear stripe phase. Yet, it is the intermediate regime that has drawn the most attention: numerous studies suggest that this region hosts a quantum spin liquid phase — a focus of intense ongoing research, where the precise nature of the ground state remains under active debate [6–8].

Understanding the ground state and excitation spectrum of such frustrated spin systems is not only of fundamental theoretical interest but is also motivated by experimental realizations in a growing number of two-dimensional materials [9–13]. However, studying these systems numerically remains a major challenge due to the exponential growth of the Hilbert space with system size. This exponential growth limits exact diagonalization studies to very small system sizes [14]. Quantum Monte Carlo methods which are capable of delivering numerically exact results, show extremely slow convergence in frustrated systems due to the infamous sign problem [15].

In this context, tensor network approaches — such as matrix product states (MPS), the density matrix renormalization group (DMRG), and related methods

— have enabled significant progress, particularly in determining ground state properties. Methods of obtaining dynamical quantities, such as the spectral function, are subject of current research.

One such development is the tangent space Krylov (TaSK) method, introduced by Kovalska *et al* [16]. This method offers a promising and computationally efficient approach for computing real-frequency spectral functions based on DMRG ground states. By constructing a Krylov subspace within the tangent space of the MPS manifold, TaSK enables direct access to spectral information without relying on analytic continuation, making it especially well-suited for computing dynamical properties in strongly correlated systems.

This thesis aims to combine both directions by applying the novel TaSK method to the triangular lattice Heisenberg antiferromagnet. Our goal is to characterize the proposed spin-liquid phase and to assess the performance of this emerging tensor network technique. In particular, we compare our results to the recent study of Drescher *et al.* [17], aiming to refine our understanding of the intermediate part of the phase diagram, and ultimately to contribute to the broader, ongoing effort to elucidate the nature of the quantum spin liquid phase.

Method

1.1 Tensor Networks - formalism

In this chapter, we introduce the tensor networks (TN) formalism as a powerful computational framework for quantum many-body systems simulation. Starting from the exponential complexity of many-body Hilbert spaces, we motivate the need for approximate representations of the wavefunctions like matrix product states (MPS), which allow to efficiently capture physical states. We present the structure and construction of MPS and matrix product operators (MPO), and describe the projector formalism used to define variational subspaces. These elements set the basis for the application of the density matrix renormalization group (DMRG) algorithm, used to obtain ground states variationally. Lastly, the tangent space krylov (TaSK) method is introduced, which is used for computing real-frequency spectral functions within the MPS tangent space.

Motivation

In condensed matter physics, it is common to consider quantum many-body systems on a lattice. They play a key role in our understanding of material properties at the microscopic level. In these systems, each vertex of the lattice hosts a local quantum degree of freedom, which may be fermionic, bosonic, or spin-like, depending on the model. These degrees of freedom are coupled by a Hamiltonian, commonly expressed in the second quantization formalism as:

$$H = \sum_{i=1}^N \hat{h}_{i,j} \quad (1.1)$$

where N is the total number of sites, $\hat{h}_{i,j}$ is a local observable centered at site i , and j is the set of sites with which the site i interacts. A system described by \hat{H} lives in an exponentially large Hilbert space \mathcal{H} of dimension d^N , where d is the number of local basis states. For example, a chain of N spin-1/2 particles has a Hilbert space of dimension 2^N . To represent an arbitrary quantum state $|\psi\rangle$ in \mathcal{H} , one must find its decomposition in the orthonormal single-particle basis $\{|\sigma_1\rangle, \dots, |\sigma_N\rangle\}$ as:

$$|\psi\rangle = \sum_{\sigma_1=1}^d \cdots \sum_{\sigma_N=1}^d \psi^{\sigma_1, \dots, \sigma_N} |\sigma_1\rangle \otimes \cdots \otimes |\sigma_N\rangle = |\boldsymbol{\sigma}\rangle \psi^{\boldsymbol{\sigma}}. \quad (1.2)$$

Such representation requires a specification of the tensor $\psi^{\boldsymbol{\sigma}}$, which corresponds to storing d^N complex values in memory. This implies that linear operations of interest, such as exact diagonalization (ED), involve $d^N \times d^N$ matrices. In practice, this is not as simple as it seems: ED is only computationally feasible for a limited size of the Hilbert space, with state-of-the-art computations performed for at most $N = 40$ sites for spin systems [18].

A natural question arises: how can many-body systems ($N \approx 10^{23}$) be efficiently simulated? Here, one needs to accept the need for approximate solutions to get to larger systems. One way is to truncate the Hilbert space to a smaller subspace of dimension $\tilde{d} < d^N$ and to approximate $|\psi\rangle$ on that smaller subspace. One can approximate $\psi^{\sigma_1, \dots, \sigma_N}$ to a product of matrices $M_i^{\sigma_i}$ of dimension $D_i \times D_m$ for a fixed σ_i , allowing us to rewrite Equation (1.2) as:

$$\begin{aligned} \psi^{\boldsymbol{\sigma}} &= [M_1]^{1\sigma_1}_{\alpha_1} [M_2]^{\alpha_1\sigma_2}_{\alpha_2} [M_3]^{\alpha_2\sigma_3}_{\alpha_3} \cdots [M_N]^{\alpha_{N-1}\sigma_N}_1 \\ &= \times_1 \begin{array}{c} M_1 \\ \uparrow \\ \sigma_1 \end{array} \rightarrow \begin{array}{c} M_2 \\ \uparrow \\ \sigma_2 \end{array} \rightarrow \begin{array}{c} M_3 \\ \uparrow \\ \sigma_3 \end{array} \cdots \begin{array}{c} M_N \\ \uparrow \\ \sigma_N \end{array} \times, \end{aligned} \quad (1.3)$$

which is the so-called *matrix product state* (MPS) representation. Diagrammatically, $M_i^{\sigma_i}$ is a generic three-legged tensor depicted as a circle with three legs (indices), where the direction of the arrows indicates their covariant (incoming) and contravariant (outgoing) nature. In the diagram (1.3), the bonds denoted by $\boldsymbol{\sigma} = \{\sigma_1, \sigma_2, \dots, \sigma_N\}$ correspond to the physical bonds and have dimension d . The connected bonds, referred to as virtual bonds, are labelled by the indices $\boldsymbol{\alpha} = \{\alpha_1, \alpha_2, \dots, \alpha_N\}$ and characterized by their bond dimension D_i . These virtual bonds encode the entanglement structure of the state. The outermost bonds, are the dummy bonds, which have dimensions $D_0 = D_N = 1$.

For simplicity, let us now assume a uniform bond dimension $D_i = D$ across all bulk sites. Under this assumption, the numerical cost of representing an MPS scales as $\mathcal{O}(ND^2d)$, since each tensor $[M_i]^{\alpha_{i-1}\sigma_i}_{\alpha_i}$ is of size $D \times d \times D$. This is exponentially more efficient than storing a generic quantum state in the full Hilbert space, which would require $\mathcal{O}(d^N)$ parameters.

The MPS representation is well-suited for ground and thermal equilibrium states of systems that satisfy the *area law* [19]. For local Hamiltonians of the form (1.1), the entanglement entropy of a state $|\psi\rangle$ between a subset of local degrees of freedom \mathcal{A} and its complement \mathcal{B} is defined as:

$$S_{\mathcal{A}(\mathcal{B})} = -\text{Tr} [\hat{\rho}_{\mathcal{A}(\mathcal{B})} \log_2 \hat{\rho}_{\mathcal{A}(\mathcal{B})}] = -\sum_{\alpha} \omega_{\alpha} \log_2 \omega_{\alpha}, \quad (1.4)$$

with ω_{α} being the eigenvalues of the reduced density matrix of $\mathcal{A}(\mathcal{B})$ obtained by tracing out the degrees of freedom of its complementary part from the density matrix: $\hat{\rho}_{\mathcal{A}(\mathcal{B})} = \text{Tr}_{\mathcal{A}(\mathcal{B})} \hat{\rho}$. For gapped systems, this entropy scales with

the boundary between the two regions: $S_{A(B)} \sim \partial A$. This behavior is known as the *area law* [20, 21]. Specifically, the entropy is constant for 1D [20], grows linearly in respect to the system size N in 2D and quadratically for 3D.

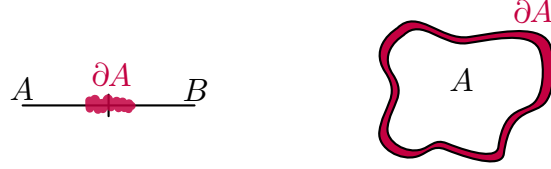


Figure 1.1: Graphical representation of the area law.

This scaling of the entanglement entropy has important consequences for the bounds on the bond dimension D needed to successfully encode the entanglement in the system. One can show that the entropy (1.4) is maximal when $\omega_\alpha = 1/D$ for all α , resulting in

$$S \leq - \sum_{\alpha=1}^D \frac{1}{D} \log_2 \frac{1}{D} = \log_2 D, \quad (1.5)$$

from which we obtain that

$$2^S \leq D. \quad (1.6)$$

From this, it follows that for 1D systems, the bond dimension D used to represent the state through an MPS, is independent of the system's size, as its entanglement entropy remains constant. This property allows for the efficient encoding of the ground state entanglement using limited numerical resources and forms the basis for many MPS-based methods, such as *density matrix renormalization group* (DMRG), which will be introduced later in this chapter.

In contrast, for 2D and 3D systems the entanglement entropy increases with system size, resulting in an exponentially growing bond dimension when using an MPS. Consequently, more advanced approaches or modifications to the TN structure are needed to keep the numerical cost manageable.

Matrix Product State basics

It is possible to obtain an MPS representation of any general tensor of arbitrary rank through sequences of matrix factorizations such as the QR decomposition or the singular value decomposition (SVD). During these factorizations, a truncation is typically performed by discarding all singular values corresponding to dimensions exceeding the desired bond dimension D .

A useful property of the MPS representation is its gauge freedom: any MPS can be written in infinitely many ways without changing the physical state it represents. This allows to transform the MPS wavefunction into four different canonical forms which are particularly advantageous for numerical algorithms. Such forms are presented in figure 1.2. In the left(right)-canonical form, all MPS tensors are left(right) isometries, defined as shown in figure 1.3. The site-canonical form is left-normalized to the left side of ℓ , right-normalized to its

right side, and has an orthogonality center at a reference site ℓ . Lastly, the bond-canonical form, has left-normalized tensors from 1 to ℓ and right-normalized one from $\ell + 1$ to N .

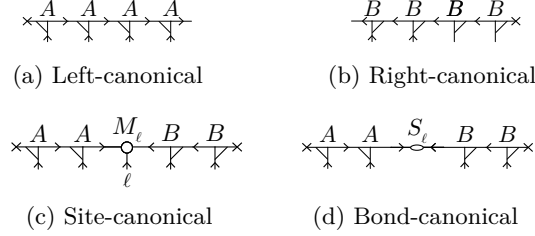


Figure 1.2: Diagrammatic representation for various canonical forms of the MPS representation.

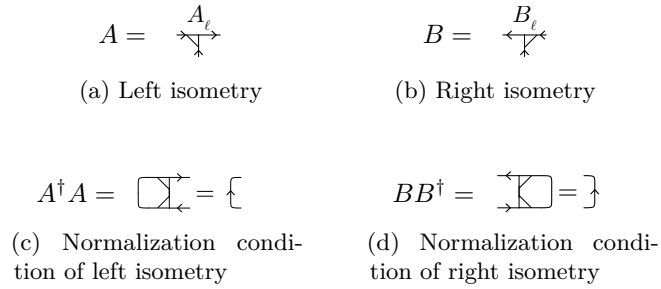


Figure 1.3: Diagrammatic representation of isometry conditions.

The MPS representation also offers powerful contraction schemes. For example, the overlap between two MPS states can be computed by contracting all the physical indices site by site, while successively contracting the corresponding virtual bonds between neighboring tensors:

$$\begin{aligned}
 \langle \tilde{\psi} | \psi \rangle &= [\tilde{M}_N^\dagger]^{1\sigma'_N\alpha'_N} \dots [\tilde{M}_2^\dagger]^{\alpha'_2\sigma'_2\alpha'_1} [\tilde{M}_1^\dagger]^{\alpha'_1\sigma'_1\alpha_1} [M_1]^{1\sigma_1\alpha_1} [M_2]^{\alpha_1\sigma_2\alpha_2} \dots [M_N]^{\alpha_N\sigma_N\alpha_1} \\
 &= \text{Diagrammatic representation of the contraction} \quad (1.7)
 \end{aligned}$$

The calculation of such an object becomes treatable by arranging summations in a way that minimizes the number of 'open legs':

This contraction pattern is often referred to as 'closing the zipper'. It can be performed from right to left and from left to right sides of the chain and has a total cost of $\mathcal{O}(D^3 dN)$.

Matrix Product Operator representation

Analogously to the MPS representation, a similar procedure can be used to represent any operator, for example a Hamiltonian $\hat{H} = |\sigma'\rangle H^{\sigma'}_{\sigma} \langle\sigma|$, as a product of tensors by applying a sequence of QR decompositions:

$$\hat{H} = [W_1]^{1\sigma'_1}_{\sigma_1\nu_1} [W_2]^{\nu_1\sigma'_2}_{\sigma_2\nu_2} \dots [W_N]^{\nu_{N-1}\sigma'_N}_{\sigma_N 1} = |\sigma'\rangle \left[\prod_{\ell=1}^N W_\ell \right]^{\sigma'}_{\sigma} \langle\sigma|$$

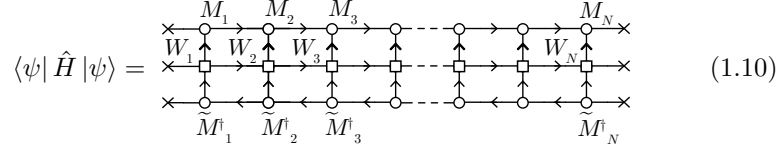
$$= \begin{array}{c} \times \rightarrow \square \rightarrow \square \rightarrow \square \rightarrow \square \rightarrow \square \rightarrow \times \\ \uparrow \quad \uparrow \quad \uparrow \quad \uparrow \quad \uparrow \quad \uparrow \\ \sigma_{\ell-1} \quad \nu_{\ell-1} \quad \nu_{\ell-1} \quad \sigma'_\ell \quad \nu_\ell \quad \sigma_\ell \\ \downarrow \quad \downarrow \quad \downarrow \quad \downarrow \quad \downarrow \quad \downarrow \\ \sigma'_\ell \quad \nu_\ell \quad \nu_\ell \quad \sigma_\ell \quad \sigma'_\ell \quad \sigma_\ell \end{array}$$

(1.9)

This operator is referred to as matrix product operator (MPO), where the four-legged tensors W_ℓ have elements $[W_\ell]^{\sigma_\ell\sigma'_\ell}_{\nu_{\ell-1}\nu_\ell}$, and the virtual bond indices ν_ℓ have dimension ω .

The contraction of an MPO with an MPS yields a new MPS, just as applying a Hamiltonian to a quantum state results in a new state. However, the resulting tensors have a higher bond dimension of $D' = D\omega \gg D$. In practice, it will always be followed by an SVD-based truncation scheme in order to bring the bond dimension down to D . A similar bond dimension increase occurs when contracting two MPOs, which likewise requires truncation to maintain computational efficiency.

Analogous to the computation of overlaps in eq. (1.7), expected values of operators can be computed in a similar manner as in eq. (1.8). The tensor network representing $\langle\psi| \hat{H} |\psi\rangle$ allows for many different contraction patterns. The most optimal pattern is shown below, with a computational cost of order $\mathcal{O}(D^3 d\omega + D^2 d^2 \omega^2)$.



$$\langle \psi | \hat{H} | \psi \rangle = \quad (1.10)$$

It is important to note that for fully local operators, the evaluation of expectation values, as given in eq. (1.10), becomes particularly efficient when the MPS is brought into its canonical form.

Projector Formalism

The projector formalism provides a systematic framework for describing and manipulating local variations of MPS within well-defined subspaces of the full Hilbert space. These projectors play a central role in a variety of tensor network algorithms, where updates are often restricted to low-dimensional tangent or variation spaces in order to ensure numerical stability and computational efficiency.

As previously discussed, when the MPS is brought into a canonical form, its tensors become isometric. Such tensors span what is known as the *kept* (κ) subspace, which contains the most relevant components and the building blocks of $|\psi\rangle$. On the other side, the *discarded* (\mathcal{D}) subspace is its orthogonal complement and captures directions along which $|\psi\rangle$ may vary, for example, during a time evolution update. Consequently, the full Hilbert space has a nested structure:

$$\mathbb{V}^{0s} \in \mathbb{V}^{1s} \in \mathbb{V}^{2s} \in \dots \in \mathbb{V}^{Ns} = \mathbb{V}. \quad (1.11)$$

\mathbb{V}^{ns} denotes the subspace containing all n -site variations of $|\psi\rangle$, with \mathbb{V}^{0s} a one-dimensional space spanned by $|\psi_0\rangle$ [22]. A notable example is \mathbb{V}^{1s} , which is the so-called tangent space of $|\psi\rangle$ and consists of all one-site variations of the state $|\psi\rangle$, endowed with a vector space structure.

Given an MPS in the site-canonical form (see figure 1.2 (c)), it is possible to define the set of left κ states $|\psi_{\ell\alpha}^K\rangle$, composed of the 1 to ℓ tensors and the set of the right *kept* states, composed of the tensors for sites $\tilde{\ell}'$ to N , $|\phi_{\tilde{\ell}'\alpha'}^K\rangle$ by using the A and B isometries shown in figure 1.3 (a) and (b) respectively. The κ and \mathcal{D} spaces form unitary maps to their parent space through $A_{\tilde{\ell}} \oplus \bar{A}_{\tilde{\ell}}$ and $B_{\tilde{\ell}} \oplus \bar{B}_{\tilde{\ell}}$, where $\bar{A}_{\tilde{\ell}}$ and $\bar{B}_{\tilde{\ell}}$ denote the \mathcal{D} isometries. This definition allows to define the following relations expressing orthonormality and completeness of the spaces:

$$\bar{A}_{\tilde{\ell}}^\dagger \bar{A}_{\tilde{\ell}} = \mathbb{I}_{\tilde{\ell}}^D, \quad A_{\tilde{\ell}}^\dagger \bar{A}_{\tilde{\ell}} = 0, \quad \bar{B}_{\tilde{\ell}'} \bar{B}_{\tilde{\ell}'}^\dagger = \mathbb{I}_{\tilde{\ell}'-1}^D, \quad B_{\tilde{\ell}'} \bar{B}_{\tilde{\ell}'}^\dagger = 0, \quad (1.12)$$

which diagrammatically corresponds to:



$$\quad (1.13)$$

The Density Matrix Renormalization Group (DMRG), introduced by Steve White in 1992 [23, 24], was originally developed to solve general quantum chain models. It has since become the standard algorithm for finding ground state solutions within the MPS ansatz. Its formulation in terms of MPS, however, was only established later in 1995 by S. Östlund and S. Rommer in the thermodynamic limit $N \rightarrow \infty$ [25], and subsequently formalized and expanded upon [26–28], as reviewed by U. Schollwöck in 2005 [29].

In its variational formulation, known as single-site (1s) DMRG, the algorithm aims to find the optimal MPS of fixed bond dimension D that minimizes the energy functional

$$E = \frac{\langle \psi | \hat{H} | \psi \rangle}{\langle \psi | \psi \rangle} \quad (1.19)$$

within the variational manifold of MPS of the given bond dimension D . This minimization is formulated by introducing a Lagrange multiplier λ and extremizing the corresponding Lagrangian:

$$\langle \psi | \hat{H} | \psi \rangle - \lambda \langle \psi | \psi \rangle, \quad (1.20)$$

graphically,

$$\langle \psi | \hat{H} | \psi \rangle - \lambda \langle \psi | \psi \rangle. \quad (1.21)$$

The main idea of DMRG is to perform this optimization iteratively, updating one tensor at a time. With $|\psi\rangle$ in site-canonical form, having a fixed site ℓ , with all other tensors being held constant, the update condition becomes:

$$\frac{\partial}{\partial C_\ell^\dagger} [\langle \psi | \hat{H} | \psi \rangle - \lambda \langle \psi | \psi \rangle] = 0 \quad \text{with} \quad \langle \psi | \psi \rangle = 1, \quad (1.22)$$

graphically,

$$= \lambda \quad (1.23)$$

This leads to an eigenvalue problem for the tensor C_ℓ that can be solved with linear algebra tools, e.g. the Lanczos algorithm [30].

To maximize efficiency, it is important that the MPS is maintained in a site-canonical form with the orthogonality center at the site ℓ . In eq. (1.20) the energy of ψ is lowered by projecting the hamiltonian \hat{H} into a local variational space associated with the site ℓ . The eigenvector with lowest eigenvalue - which corresponds to the best estimate of the ground-state energy - is used to update the MPS. This is followed by an SVD, which shifts the orthogonality center to the site $\ell + 1$, which will be the next tensor for optimization. Each optimization step is referred to as a single-site (1s) update and has a computational cost of order $\mathcal{O}(D^3 d \omega)$. To achieve global minimization of the energy E , this procedure is applied iteratively across the chain, sweeping the MPS $|\psi\rangle$ from left to right and then from right to left. These sweeps are repeated until the change in energy between successive iterations is below some predefined convergence threshold. An alternative approach is the two-site (2s) DMRG algorithm, in which the energy minimization is performed over two neighboring MPS tensors simultaneously. This enlarges the local variational space allowing for dynamic adjustment of the bond dimension during the optimization. Note that since DMRG scales with order $\mathcal{O}(D^3)$ it is useful to start the computations with low D and gradually increase it while sweeping.

Controlled Bond Expansion

When symmetries are present, the ground-state search must allow for the possibility of expanding the virtual bond spaces, which encode symmetry-related information, whenever such expansion leads to a lower energy. Single-site (1s) DMRG algorithms can often become trapped in metastable states due to their fixed bond dimension. In contrast, two-site (2s) DMRG allows for bond dimension growth, avoiding such traps. However, this flexibility comes at a significantly higher computational cost, i.e. $\mathcal{O}(D^3 d^3 + D^3 d^2 \omega)$.

To address this, Gleis *et al.* [31] introduced the Controlled Bond Expansion (CBE) algorithm that combines the efficiency of single-site DMRG, with the flexibility of bond-expansion growth. This approach allows the MPS to escape local minima and achieve better convergence to the ground state, while maintaining 1s computational costs.

In 2s DMRG, the MPS is brought into a bond-canonical form and the \hat{H} is expressed as:

$$\hat{H}_\ell^{1s} = \mathcal{P}_\ell^{1s} \hat{H} \mathcal{P}_\ell^{1s} = \left[\begin{array}{c} \rightarrow \quad \uparrow \quad \leftarrow \\ \rightarrow \quad \square \quad \leftarrow \\ \leftarrow \quad \uparrow \quad \rightarrow \end{array} \right] H_\ell^{1s} \quad (1.24)$$

$$\hat{H}_\ell^{2s} = \mathcal{P}_\ell^{2s} \hat{H} \mathcal{P}_\ell^{2s} = \left[\begin{array}{c} \rightarrow \quad \uparrow \quad \rightarrow \quad \uparrow \quad \leftarrow \\ \rightarrow \quad \square \quad \rightarrow \quad \square \quad \leftarrow \\ \leftarrow \quad \uparrow \quad \leftarrow \quad \uparrow \quad \rightarrow \end{array} \right] H_\ell^{2s} \quad (1.25)$$

The optimization procedure closely resembles that of 1s DMRG but operates in a larger effective Hilbert space that includes variations in the discarded sectors.

The key insight in CBE is to identify the components of the two-site orthogonal space that carry significant weight in the energy reduction. These components are denoted as the 'relevant' discarded space, denoted rDD . They can be found via a projector that can be constructed at one-site costs through a truncation scheme termed 'shrewd selection' [31].

To facilitate robust convergence, in this thesis we employ the CBE algorithm in combination with a mixing parameter α [32] (for more details, see S.3 of the reference [31]). The use of the latter in the context of (2s) DMRG schemes is well-established [33]. By introducing noise into the wavefunction, the mixing term enables the system to escape metastable minima. Including it during the first few DMRG sweeps, in conjunction with the CBE algorithm, has been shown to be the optimal strategy [31, 34] when simulating particularly challenging models, such as those exhibiting quantum spin behavior.

1.3 Tangent space Krylov (TaSK) scheme

Introduced by O. Kovalska *et al.* [16], the tangent space Krylov (TaSK) method provides an accurate and computationally efficient approach for calculating real-frequency spectral functions based on ground states obtained via DMRG. The spectral function is defined as:

$$S(\mathbf{k}, \omega) = -\frac{1}{\pi} \text{Im} \langle \psi_0 | \hat{O}_{\mathbf{k}} \frac{1}{\omega + i\eta + E_0 - \hat{H}} \hat{O}_{\mathbf{k}}^\dagger | \psi_0 \rangle. \quad (1.26)$$

Where the operator $\hat{O}_{\mathbf{k}}$ typically adds or removes a particle with momentum \mathbf{k} . In the context of this thesis, it corresponds to a spin operator in momentum space:

$$\hat{O}_{\mathbf{k}} = \hat{S}_{\mathbf{k}} = \frac{1}{\sqrt{N}} \sum_j e^{-i\mathbf{k} \cdot \mathbf{r}_j} \hat{S}_j. \quad (1.27)$$

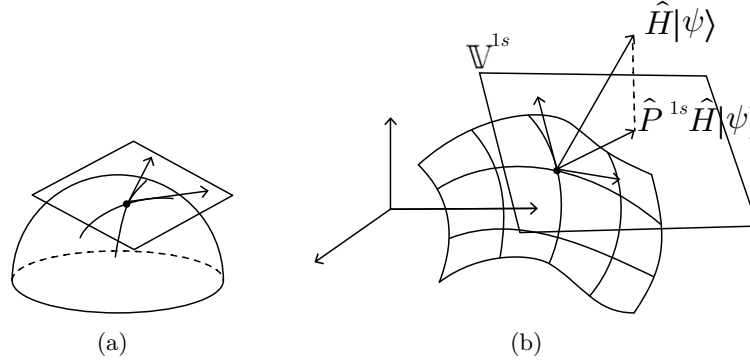


Figure 1.4: (a) Illustration of a tangent space spanned by vectors tangent to curves within a smooth geometric structure (b) The MPS manifold M_{MPS} , embedded in the full Hilbert space \mathbb{V} of dimension d^N ; \mathbb{V}^{1s} indicates the tangent space of single-site variations within this manifold.

The core idea behind TaSK is to confine the computations to the tangent space of the ground state MPS $|\psi_0\rangle$. To initiate the method, one applies the momentum-space operator $\hat{O}_{\mathbf{k}}$ to the ground state. The resulting state, $|\psi_1\rangle$, belongs to the tangent space \mathbb{V}^{1s} of $|\psi_0\rangle$ since $\hat{O}_{\mathbf{k}}$ is a linear combination of local operators, acting on a single site.

$$|\psi_1\rangle = \hat{O}_{\mathbf{k}} |\psi_0\rangle = \sum_{\ell=1}^N \times \text{---} \text{---} \text{---} \overset{T^\ell}{\underset{\ell}{\bullet}} \text{---} \text{---} \text{---} \times, \quad (1.28)$$

Where $T^\ell = \text{---} \text{---} \text{---} \overset{\bullet}{\underset{\ell}{\text{---}}} \text{---} \text{---}$ are rank-3 tensors contracted with the Schmidt states of $|\psi_0\rangle$, with $T^N = \text{---} \text{---} \text{---} \overset{\bullet}{\text{---}} \text{---} \text{---}$ and $T^\ell = \text{---} \text{---} \text{---} \overset{\bullet}{\underset{\ell}{\text{---}}} \text{---} \text{---}$ for $\ell < N$. This is known as a quasiparticle ansatz [35–40]. To compute the spectral function, we construct a Krylov subspace starting from the initial tangent space vector $|\psi_1\rangle$ using a standard Lanczos algorithm [30]:

$$\mathcal{K}(\psi_1) = \text{span}\{|\psi_1\rangle, H^{1s}|\psi_1\rangle, \dots, (H^{1s})^{\mathcal{N}_{\text{kr}}}|\psi_1\rangle\}. \quad (1.29)$$

Here, the effective Hamiltonian, $H^{1s} = \mathcal{P}^{1s} H \mathcal{P}^{1s}$, corresponds to the projection of \hat{H} (expressed as an MPO) into the subspace \mathbb{V}^{1s} . This is crucial, since the above scheme is only stable due to the inherent vector space structure of \mathbb{V}^{1s} . The result is an $\mathcal{N}_{\text{kr}} + 1$ dimensional Krylov space, on which \hat{H}^{1s} has a tridiagonal form that allows for efficient diagonalization, enabling the resolution of the excitations needed to evaluate $S(\mathbf{k}, \omega)$.

An error measure can be computed to estimate the error coming from the projection of the Hamiltonian into the subspace \mathbb{V}^{1s} . This error arises from the implicit assumption that the elementary excitations of \hat{H} can be fully resolved within this subspace. By considering a two-site projector (1.18), one can compute a 2s contribution to the energy variance, providing a measure of the magnitude of the neglected component of the state within the two-site variational space \mathbb{V}^{2s} as $\Delta_E^{2\perp} = \|\mathcal{P}^{2\perp} H\psi\|^2$, with the $\mathcal{P}^{2\perp}$ projector defined as:

$$\mathcal{P}^{2\perp} = \mathcal{P}^{2s} - \mathcal{P}^{1s} = \sum_{\ell=1}^{N-1} \begin{array}{c} \text{---} \times \text{---} \text{---} \times \text{---} \\ \text{---} \text{---} \times \text{---} \text{---} \times \text{---} \\ \text{---} \times \text{---} \text{---} \times \text{---} \end{array} \quad \begin{array}{c} \text{---} \times \text{---} \text{---} \times \text{---} \\ \text{---} \text{---} \times \text{---} \text{---} \times \text{---} \\ \text{---} \times \text{---} \text{---} \times \text{---} \end{array} \quad \ell \quad \ell+1 \quad . \quad (1.30)$$

This error depends on the quality of the ground-state approximation and will systematically decrease with increasing bond dimension D of the respective ground state MPS.

Theoretical Background

2.1 J_1 - J_2 Triangular Lattice Antiferromagnetic Heisenberg Model

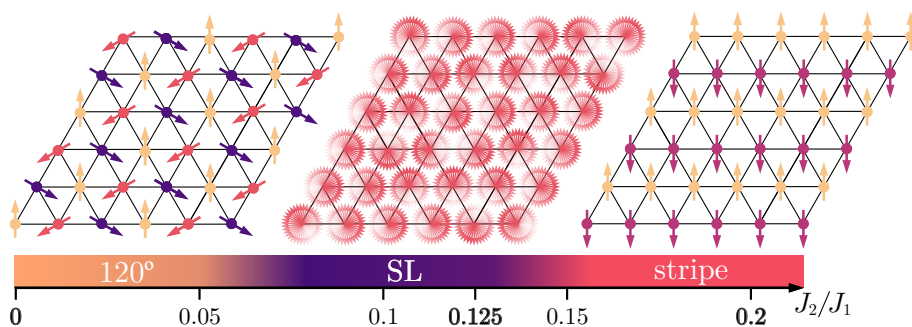


Figure 2.1: A schematic phase diagram of the J_1 - J_2 triangular-lattice Heisenberg antiferromagnetic model as a function of the next-nearest-neighbor coupling J_2 . The diagram illustrates the evolution from the 120° Néel-ordered phase at $J_2 = 0$, through the intermediate spin-liquid candidate region, and into the stripe-ordered phase at larger J_2 .

The Heisenberg model is one of the most fundamental and widely studied models in quantum magnetism. In its simplest form, it describes localized spins interacting via an exchange coupling, typically denoted by J_1 , between nearest-neighbors (NN) in a lattice. For the antiferromagnetic (AFM) case ($J_1 > 0$) on a triangular lattice, the ground state has been established to have a 120° Néel order phase [41–43]. Despite its apparent simplicity, the geometry of the triangular lattice provides a clean platform for the emergence of a quantum spin liquid (QSL) when further interactions are introduced.

By including a next-nearest neighbor (NNN) exchange coupling J_2 , frustration in the spin system is increased (see figure 2.2), which can destabilize the Néel order and open a window for quantum spin liquid behavior.

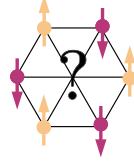


Figure 2.2: Schematic representation of geometric frustration in the triangular lattice. Antiferromagnetic interactions on the edges of a triangle lead to competing constraints, preventing all spin pairs from simultaneously minimizing their interaction energy.

The resulting Hamiltonian reads:

$$\hat{H} = J_1 \sum_{\langle i,j \rangle} \hat{\mathbf{S}}_i \cdot \hat{\mathbf{S}}_j + J_2 \sum_{\langle\langle i,j \rangle\rangle} \hat{\mathbf{S}}_i \cdot \hat{\mathbf{S}}_j \quad (2.1)$$

where $\hat{\mathbf{S}}_i$ is a spin-1/2 operator acting on site i , and $\langle i,j \rangle$ and $\langle\langle i,j \rangle\rangle$ denote NN and NNN pairs on the triangular lattice, respectively. The frustrated interaction plays a crucial role in the suppression of magnetic order and the possible stabilization of QSL phases [44]. In the classical limit, this model exhibits a zero-temperature phase transition at $\frac{J_2}{J_1} = 1/8$ [3, 6, 45] between the 120° Néel order and a four-sublattice ordered phase with a residual degeneracy.

Many numerical studies have been performed for the quantum model, hinting at the presence of a QSL phase in the region around the classical transition point followed by a collinear stripe-ordered phase for larger J_2 values. The boundaries of the QSL phase have been investigated using a variety of computational and analytical methods, yielding a range of estimates. For instance, Variational Monte Carlo (VMC) calculations suggest a QSL region within $0.08 \lesssim J_2/J_1 \lesssim 0.16$ [6], DMRG numerics [7] set the range $0.07 < J_1/J_2 < 0.15$ while series expansion methods [46] suggest $0.06 < J_1/J_2 < 0.17$ or the values $0.072 < J_1/J_2 < 0.18$ through random phase approximation [45]. The precise nature of this QSL phase remains under active debate [6–8, 47–50], with the most popular candidates being a gapped \mathbb{Z}_2 or a gapless U(1) Dirac spin liquid.

2.2 Candidate Spin Liquid Phases

What is a quantum spin liquid (QSL)? The term originated from Anderson’s seminal 1973 paper, where he proposed that the ground state of a frustrated antiferromagnet could be a quantum disordered state — what he called a *resonating valence bond* (RVB) state [51]. Since then, spin liquids have become a central topic in condensed matter physics, bridging magnetism, quantum topology and quantum information science.

The definition of a QSL has evolved over the decades as our understanding of strongly correlated systems has deepened. Within the modern framework, a QSL is defined to be an exotic phase of matter that lacks any form of magnetic order even at zero temperature, despite strong spin-spin correlations [1, 44, 52].

While classical spin liquids arise from extensive ground-state degeneracy and geometric frustration, their quantum counterparts emerge through strong quantum fluctuations — often in low-dimensional, frustrated magnetic systems.

Quantum spin liquids (QSLs) are characterized by long-range entanglement and the absence of conventional symmetry breaking. Unlike magnetically ordered phases, they exhibit non-local correlations, and their classification frequently involves emergent internal gauge structures such as $SU(2)$, $U(1)$, or \mathbb{Z}_2 . These gauge fields can give rise to topological order and are often associated with the presence of fractionalized excitations, such as spinons.

Such characteristics can be used to classify different kinds of QSLs. While this classification remains an active area of research, QSLs are often distinguished according to several features: the nature of the emergent gauge field (e.g. $SU(2)$, $U(1)$ or \mathbb{Z}_2), the excitation spectrum (gapped or gapless), the presence or absence of topological order, and symmetry properties such time-reversal or lattice symmetries [1, 44, 52, 53].

These categories are not mutually exclusive and often overlap. For example, a Dirac SL is typically gapless, exhibiting algebraically decaying correlations and an emergent $U(1)$ gauge structure [53]. On the other side, a \mathbb{Z}_2 SL is typically gapped, topologically ordered, and features fractionalized excitations such as spinons [1]. The latter arise from the system's highly entangled ground state and can be indirectly observed through inelastic neutron scattering (INS) experiments [54] (which probe the dynamic spin structure factor of the system) on which they appear as a broad continuum of excitations. In contrast, conventional magnets support magnons, spin-1 quasiparticles that correspond to collective spin-wave excitations of an ordered state [55], which appear as sharp dispersive modes.

Experimental Landscape

Since Anderson's proposal of the RVB state in 1973 [51], the search of experimental realizations of spin liquids has remained a central challenge in condensed matter physics [44]. A major breakthrough came in 2003, when an organic Mott insulator, $\kappa - (\text{BEDT} - \text{TTF})_2\text{Cu}_2(\text{CN})_3$, with quasi-triangular lattice, was found to exhibit no magnetic order even at tens of mK - a temperature far below the energy scale of the exchange interactions [9]. This discovery renewed the interest in triangular-lattice systems as promising QSL candidates and also broadened the exploration of other frustrated geometries such as kagome and hyperkagome lattices [10].

Recent progress has been made using inorganic rare-earth-based triangular-lattice compounds, which offer cleaner platforms with large spin-orbit coupling and strong quantum fluctuations [11]. Amongst them, the NaYbCh_2 ($\text{Ch} = \text{O}, \text{S}, \text{Se}$) family has emerged as a leading QSL candidate.

In particular, Scheie *et. al.* [56], performed neutron scattering experiments on NaYbSe_2 , and observed a broad continuum of excitations, consistent with spin fractionalization. No static magnetic order was detected down to 100 mK and AC susceptibility measurements revealed a spin gap of approximately $2.1 \mu\text{eV}$. These results rule out gapless $U(1)$ Dirac QSLs and suggest a gapped \mathbb{Z}_2 spin liquid ground state. This interpretation is supported by magnetic dilution experiments performed by Zhang *et. al.* [13], who extracted anisotropic exchange parameters in $\text{NaYb}_{0.02}\text{Lu}_{0.98}\text{Se}_2$. Their results are consistent with an easy-plane XXZ Hamiltonian, which is known to stabilize \mathbb{Z}_2 spin liquids in frustrated triangular-lattice systems.

Other materials have shown similar behavior. In YbMgGaO_4 , Li, et. al. [10] found evidence for spin-liquid-like dynamics extending beyond NN. However, the role of structural disorder remains a concern. It is still under debate whether the fractionalized excitations are truly generic for all triangular magnets or whether structural disorder plays any important role [10].

Although inorganic compounds offer structurally clean platforms for studying QSLs, organic materials have also played a significant role in the development of the field. One example is $\beta' - \text{EtMe}_3\text{Sb}[\text{Pd}(\text{dmit})_2]_2$, a triangular-lattice material that has attracted attention for exhibiting a linear specific heat even though being an insulator. This was initially interpreted as evidence for a gapless SL. However, recent electron spin resonance (ESR) and muon spin relaxation (μSR) experiments revealed its behavior is dominated by quasi-1D dynamics, rather than the expected 2D characteristics [12]. These findings highlight the importance of using advanced spectroscopic techniques to resolve the true nature of candidate QSLs. The authors also emphasize the relevance of this search for potential applications in quantum computing and spintronic technologies.

Overall, recent advances highlight both the potential and difficulty of identifying QSLs. While materials like NaYbSe_2 show strong evidence for spin-liquid behavior, challenges such as disorder and hidden dimensionality persist. Continued progress will rely on high-quality materials and complementary experimental techniques.

Results

This chapter presents the main results of our study and discusses the physical insights that emerge from them. We begin by introducing the physical systems investigated, the key parameters considered, and other relevant methodological aspects necessary for interpreting the results.

We then present the principal observables used to characterize the different ground state behaviors: the equal-time spin structure factor, the spin-spin correlation functions, and, most importantly, the spectral functions obtained via the TaSK algorithm. Each observable is introduced with a brief discussion of its physical significance.

The chapter is structured to follow a logical progression from setup to interpretation. After outlining the systems and observables, we present the core numerical results, with a focus on representative values of the interaction parameter J_2 (see chapter (2)). Special attention is given to identifying signatures of quantum spin liquid behavior, with the goal of contributing new insights into this widely studied and debated phase in the triangular-lattice Heisenberg antiferromagnet.

3.1 Preliminary considerations

To systematically explore the evolution of the ground state along the three distinct regimes of the THLAF (see chapter (2)), we proceed by analyzing the observables at three key values of J_2 . We begin with the unfrustrated case $J_2 = 0$, which serves as a reference point and allows us to verify that our approach reproduces known features of the conventional 120° Néel order. We then turn to $J_2 = 0.125$, which lies in the quantum spin liquid candidate regime, and is of particular interest for detecting possible signatures of spin liquid behavior. Concretely, the point $J_2 = 0.125$ corresponds to the classical phase transition point and lies deep within the candidate quantum spin liquid region, predicted by various methods such as DMRG, VMC or series expansion [6, 7, 45, 46]. Finally, for completeness, we include results at $J_2 = 0.2$, corresponding to a more strongly frustrated regime, to observe whether the trends identified at intermediate frustration persist or evolve further.

Before performing numerical simulations, a specific choice of lattice geometry and boundary conditions must be made, as they directly influence finite-size

effects and our ability to capture relevant physical properties in two-dimensional systems.

Cylindrical wrapping

The DMRG algorithm is highly efficient when applied to one-dimensional systems (see section (1.2)). To extend its use to two-dimensional models, a common approach involves mapping the 2D lattice onto a one-dimensional chain. This is typically achieved by defining a *snake-like* path that traverses all lattice sites, reordering them into a linear sequence. A key consequence of this mapping is that short-range interactions in the original two-dimensional geometry may become long-range along the one-dimensional path, thereby increasing the complexity of the Hamiltonian representation.

In our study, we consider a cylindrical geometry, introducing periodic boundary conditions (PBC) along the circumference and open boundary conditions (OBC) along the cylinder's length. This setup provides a good approximation of a two-dimensional system, as it removes edge effects along the periodic direction while remaining computationally manageable with DMRG.

As discussed in section (1.1), two-dimensional systems obey an area law for entanglement entropy, where the entropy between two regions scales with the length of their shared boundary. In the context of a cylinder, this corresponds to a cut across the width. Under snake-like mapping, such a cut typically corresponds to a single MPS bond. As a result, the entanglement entropy across MPS bonds increases with the cylinder's width, leading to an exponential growth in the bond dimension required to accurately represent the ground state. In contrast, the dependence on the cylinder's length is much weaker. Consequently, while DMRG remains efficient for narrow cylinders, the computational cost grows rapidly with increasing width.

In the following, we present the so-called YC wrapping [8] with three distinct cylindrical boundary conditions, which effectively correspond to identifying the site labeled 'x' with either site 'a', 'b', or 'c' shown in figure 3.1.

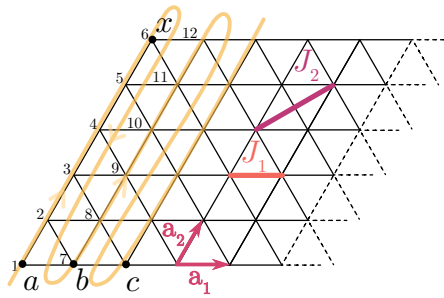


Figure 3.1: Triangular lattice structure with the snake-like path shown, illustrating the site ordering used for the one-dimensional chain mapping. Sites labeled x , a , b , and c are used to demonstrate the three distinct wrapping types discussed in the text. Primitive lattice vectors \mathbf{a}_1 and \mathbf{a}_2 are indicated, along with nearest-neighbor couplings J_1 and next-nearest-neighbor couplings J_2 .

To succinctly label these different cylindrical wrapping types, we use the notation $YCL_y - u - L_x$. Here, the index u specifies the boundary condition

by identifying sites \mathbf{r} and $\mathbf{r} + L_y \mathbf{a}_2 - u \mathbf{a}_1$, and L_y and L_x correspond to the number of spins along the circumference and length of the cylinder, respectively. The vectors \mathbf{a}_1 and \mathbf{a}_2 are the primitive vectors of the Bravais lattice and \mathbf{r} denotes the position of a lattice site. In our case, we will consider the cases with YCL_y-0-L_x , YCL_y-1-L_x , and YCL_y-2-L_x which correspond to ' $a-x$ ', ' $b-x$ ', and ' $c-x$ ' wrapping types respectively in figure 3.1.

Once the appropriate geometry is chosen, a snake-like path is defined to map the two-dimensional lattice onto a one-dimensional chain, as illustrated in figure 3.1. Careful consideration must be given to both the geometry and the path, as each introduces approximations—especially in systems where the geometry significantly influences the physical behavior. In particular, the choice of mapping strongly affects the number and range of effective couplings in the one-dimensional representation. An ill-chosen path can lead to many artificially long-range interactions, which increase the computational cost without introducing any new information. Minimizing such couplings is therefore essential for both numerical efficiency and physical accuracy.

In this thesis, we focus our work on the YCL_y-0-L_x geometry, with $L_y = 6$ and $L_x = 36$ respectively. All results refer to this wrapping convention.

Consequences of the cylinder choice

The choice of cylindrical geometry does not only impact entanglement and finite-size effects; it also determines the set of momentum modes accessible to the system. Since DMRG simulations are performed on finite cylinders with periodic boundary conditions in one direction, the translational symmetry is preserved only partially. As a result, momentum is no longer a good quantum number in general, but discrete momentum components can still be defined along the periodic direction.

This restriction plays an important role when computing observables such as the equal-time structure factors, spectral functions or identifying ordering patterns in momentum space. In particular, it limits the ability of the system to capture certain key features of the full two-dimensional Brillouin zone. The specific set of allowed momenta depends directly on the wrapping of the cylinder and the corresponding identification of lattice sites.

To formalize this, we turn to Bloch's theorem [57], which states that imposing periodic boundary conditions constrains the wavefunction to be invariant under discrete lattice translations. In our case, the periodic identification implies:

$$\begin{aligned} \psi(\mathbf{r}) &= \psi(\mathbf{r} + L_y \mathbf{a}_2 - n \mathbf{a}_1) \\ \Rightarrow e^{i\mathbf{k} \cdot \mathbf{r}} &= e^{i\mathbf{k} \cdot (\mathbf{r} + L_y \mathbf{a}_2 - n \mathbf{a}_1)} = e^{i\mathbf{k} \cdot \mathbf{r}} \cdot e^{i\mathbf{k} \cdot (L_y \mathbf{a}_2 - n \mathbf{a}_1)}. \end{aligned} \quad (3.1)$$

The momentum vector is expressed in terms of the reciprocal lattice basis as $\mathbf{k} = k_1 \mathbf{b}_1 + k_2 \mathbf{b}_2$ where \mathbf{b}_1 and \mathbf{b}_2 are the reciprocal lattice vectors corresponding to the real-space primitive vectors \mathbf{a}_1 and \mathbf{a}_2 of the triangular lattice (see figure 3.1). The reciprocal vectors are given by:

$$\mathbf{b}_1 = 2\pi \frac{\mathbf{Qa}_2}{\mathbf{a}_1 \cdot \mathbf{Qa}_2}; \quad \mathbf{b}_2 = 2\pi \frac{\mathbf{Qa}_1}{\mathbf{a}_2 \cdot \mathbf{Qa}_1} \quad (3.2)$$

where $\mathbf{a}_1 = [a, 0]$ and $\mathbf{a}_2 = [a/2, \sqrt{3}/2]$. The lattice constant is set to $a = 1$ and \mathbf{Q} corresponds to the 90° rotation matrix.

Applying the periodicity condition leads to the quantization of momentum components along the periodic direction:

$$e^{i\mathbf{k} \cdot (L_y \mathbf{a}_2 - n \mathbf{a}_1)} = e^{i2\pi m} \quad \text{with } m = 0, 1, 2, \dots, L_y - 1. \quad (3.3)$$

Figure 3.2 illustrates the resulting discrete sets of allowed momenta in the Brillouin zone for the three cylindrical wrappings used in this work as well as for an infinite two-dimensional lattice. These wrappings constrain which momenta are accessible in our simulations and therefore influence the observables we can extract. For example, if a particular cylinder does not intersect high-symmetry points such as the K point, key features of the system's low-energy behavior may remain hidden. This underlines the importance of a careful choice of boundary conditions and geometry. An example of a poor choice would be to take the YCL_y-1-L_x and YCL_y-2-L_x geometries to study the K or M points, see figure 3.2. An interesting feature for the YCL_y-2-L_x geometry, though, is that the allowed momenta go through the Dirac points. We present some results on this geometry in Appendix B. However, we don't expect to find any special features in the dynamical structure factor, explained below, at that point.

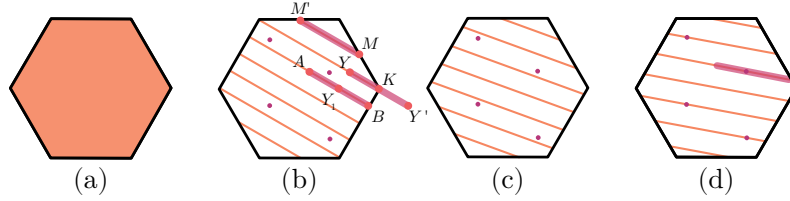


Figure 3.2: Accessible momenta for the triangular lattice on cylindrical geometries. (a) Allowed momenta in the infinite 2D Brillouin zone. (b)–(d) Allowed momenta for the finite-width cylinders $YC6-0-L_y$, $YC6-1-L_y$, and $YC6-2-L_y$, respectively. In (b) and (d), the momentum paths along which spectral data is computed are highlighted. High-symmetry points along these paths are marked with dots and labeled. The Dirac points, located at $\pm \mathbf{Q} = \pm(\pi/2, \pi/(2\sqrt{3}))$, are shown in purple.

In this work, we adopt the same momentum-space cuts as those used by Drescher *et al.* in [17], in order to benchmark the performance of our TaSK algorithm against established results. Specifically, we focus along three distinct paths in the Brillouin zone: from A to B , from Y to Y' , and from M' to M , passing through the high-symmetry point K , shown in figure 3.2(b). This choice enables a direct and meaningful comparison of dynamical signatures. In addition, in Appendix B some results for the $YC6-2-36$ and the cut shown in figure 3.2 are presented.

3.2 Physical Observables: Definitions

To characterize the ground state properties of the system across different parameter regimes, we compute a set of physical observables that probe both

local and non-local correlations. These observables serve as diagnostic tools to identify the presence or absence of magnetic order, detect symmetry-breaking patterns, and reveal signatures of exotic phases such as quantum spin liquids. In this section, we aim to define the key quantities used throughout the analysis.

Real-Space and Momentum-Space Spin Correlations

As previously discussed, the TLHAF serves a paradigmatic example of a frustrated quantum magnet (2). To investigate the nature of the ground state and the evolution of magnetic ordering across different coupling regimes, we would like to compute the real-space spin-spin correlation function:

$$S_{ij} = \langle \hat{\mathbf{S}}_i \cdot \hat{\mathbf{S}}_j \rangle \quad (3.4)$$

where i and j denote sites of the triangular lattice. This observable provides insight into how spin orientations are correlated — whether they tend to align, anti-align or fluctuate independently. A negative value on a give bond indicates antiferromagnetic correlations, while a positive value shows ferromagnetic correlations. Such behavior helps distinguish between magnetically ordered and disordered (e.g., spin liquid) phases. In this work, we will focus on nearest-neighbor spin-spin correlations.

To gain a complementary perspective, it is instructive to analyze the correlations in momentum space via their Fourier transform. This yields the equal-time structure factor (ETSF), which encodes how spin correlations are distributed accross different momentum modes and provides clearer signatures of emerging magnetic order or the absence thereof. It is defined as:

$$\chi(\mathbf{k}) = \frac{1}{N} \sum_{i,j} e^{-i\mathbf{k} \cdot (\mathbf{r}_i - \mathbf{r}_j)} \langle \hat{\mathbf{S}}_i \cdot \hat{\mathbf{S}}_j \rangle, \quad (3.5)$$

where (k) is the momentum vector in the Brillouin zone, \mathbf{r}_i denotes the position of site i , and N is the total number of lattice sites. The vector difference $(\mathbf{r}_i - \mathbf{r}_j)$ is taken to be the minimal distance between sites i and j , accounting for periodic boundary conditions when applicable.

The equal-time structure factor $\chi(\mathbf{k})$ provides momentum-resolved information about spin correlations and is evaluated at the set of discrete allowed momentum vectors \mathbf{k} , which are determined by the specific boundary conditions imposed on the lattice geometry (see 3.1). Through the equal-time structure factor, one can also compute the order parameter for a given momentum $m^2 = \chi(\mathbf{k})/N$.

Spectral Functions

The retarded Green's function for a spin model describes how a spin excitation propagates through a system after a perturbation and it is defined as:

$$G_R(\mathbf{k}, \omega) = -i \int_0^\infty dt e^{i\omega t} \langle \psi_0 | [\hat{\mathbf{S}}_{-\mathbf{k}}(t), \hat{\mathbf{S}}_{\mathbf{k}}(0)] | \psi_0 \rangle \quad (3.6)$$

where the momentum-space spin operators are defined as:

$$\hat{\mathbf{S}}_{\mathbf{k}} = \frac{1}{\sqrt{N}} \sum_j e^{-i\mathbf{k} \cdot \mathbf{r}_j} \hat{\mathbf{S}}_j, \quad (3.7)$$

with $\hat{\mathbf{S}}_j$ being the local spin-1/2 operator at site j , \mathbf{k} the crystal momentum and \mathbf{r}_j the position of site j , and have Hermitian conjugate $\hat{\mathbf{S}}_{\mathbf{k}}^\dagger = \hat{\mathbf{S}}_{-\mathbf{k}}$. This operators describe a collective spin fluctuation mode at momentum \mathbf{k} , creating for example, a magnon or a spinon pair. It probes spin correlations in the reciprocal space, which is what experiments like neutron scattering measure.

At zero temperature, we can express the Green's function (3.6) through the Lehmann representation:

$$G_R(\mathbf{k}, \omega)|_{T=0} = \sum_{\beta} \left[\frac{|\langle \psi_0 | \hat{\mathbf{S}}_{\mathbf{k}} | \beta \rangle|^2}{\omega + i\eta - (E_{\beta} - E_0)} - \frac{|\langle \psi_0 | \hat{\mathbf{S}}_{\mathbf{k}}^\dagger | \beta \rangle|^2}{\omega + i\eta + (E_{\beta} - E_0)} \right] \quad (3.8)$$

where $\{|\beta\rangle\}$ is a complete set of eigenstates of the Hamiltonian H with corresponding eigenenergies E_{β} . It accounts to the response of the system to an injected spin excitation. Each term corresponds to the contribution of a physical spin-excited state $|\beta\rangle$ to the dynamics. Taking its imaginary part, we obtain an observable known as dynamical structure factor (DSF):

$$S(\mathbf{k}, \omega) = -\frac{1}{\pi} \text{Im} G_R(\mathbf{k}, \omega)|_{T=0} = \sum_{\beta} \left[|\langle \beta | \hat{\mathbf{S}}_{\mathbf{k}} | \psi_0 \rangle|^2 \delta(\omega - (E_{\beta} - E_0)) + |\langle \beta | \hat{\mathbf{S}}_{\mathbf{k}}^\dagger | \psi_0 \rangle|^2 \delta(\omega + (E_{\beta} - E_0)) \right]. \quad (3.9)$$

By restricting $\omega > 0$, i.e. considering only absorption:

$$S(\mathbf{k}, \omega) = \sum_{\beta} |\langle \beta | \hat{\mathbf{S}}_{\mathbf{k}} | \psi_0 \rangle|^2 \delta(\omega - (E_{\beta} - E_0)), \quad \omega > 0 \quad (3.10)$$

which quantifies the probability of exciting the system from the ground state $|\psi_0\rangle$ to an eigenstate $|\beta\rangle$, with an energy transfer $\omega = E_{\beta} - E_0$, via a spin fluctuation at momentum \mathbf{k} . As such, it provides a direct probe of the nature of low-energy excitations in the system. In magnetically ordered phases, the dominant excitations are typically gapless magnons, while in quantum disordered phases such as spin liquids, the excitations may be fractionalized spinons [48].

Spectral functions are obtained in a discrete form from the TaSK method. For our results, we apply a continued fraction expansion (CFE) to this discrete data, preserving $2 \times N_{\text{CFE}} = 4$ spectral moments. A Gaussian broadening with $\sigma = 0.4$ is used to obtain smooth spectra.

Ground State Convergence

The determination of the ground state is a fundamental step towards the study of the different properties of our system. To do so, we employ the CBE-DMRG algorithm using the QSpace tensor library [58–60], which enables the explicit incorporation of the $SU(2)$ symmetry throughout this work. The use of non-Abelian symmetries ensures that the calculations respect rotational invariance and also improves numerical efficiency and precision by compressing the Hilbert space into symmetry multiplets.

In the following, we aim to present the convergence protocol for obtaining accurate ground states in the systems studied. Two main factors limit the precision of the computed ground state: the bond dimension and the number of sweeps. To ensure convergence, we run CBE-DMRG with increasing bond dimensions. At each step, we initialize the simulation with the MPS obtained from the previous bond dimension. This warm-start strategy significantly accelerates convergence in subsequent steps of the algorithm. However, the initialization of the first CBE-DMRG step requires a choice of an MPS ansatz. It is important to point out that such a choice can implicitly restrict the evolution to certain symmetry sectors if not chosen carefully. To address this, in the quantum spin liquid candidate phase, we randomized the initial MPS ansatz to avoid any unintentional bias toward a specific symmetry sector. We then performed multiple CBE-DMRG runs with this randomized initialization, using the same sweep schedule for each run, to test whether different initial states could converge to different ground states.

To stabilize the optimization process and improve convergence, we activate the α -mixing parameter during the initial stages of the calculation [61]. Specifically, we turn on the mixing parameter for the entire duration of the first bond dimension runs, and subsequently apply it only during the first two sweeps of each higher bond dimension. A fixed number of sweeps is performed at each bond dimension to ensure that the state has sufficiently relaxed. The parameters used in this procedure are summarized in Table 3.1.

Bond Dimension	Number of Sweeps	Number of Sweeps with α -mixing Active
512	16	16
1024	16	2
2048	8	2
3000	7	2

Table 3.1: DMRG sweep schedule used for the simulations. Each sweep consists of a full back-and-forth pass through the system. The rightmost column indicates how many of those sweeps used an active α -mixing parameter.

In figure 3.3 we aim to show this process, showing how the energy per site varies after every sweep and when increasing the bond dimension. Having established the convergence protocol and numerical framework for reliably obtaining the ground states, we now proceed to present the results for our simulations. In the following, we will analyze the ground state properties of the system for various values of J_2 .

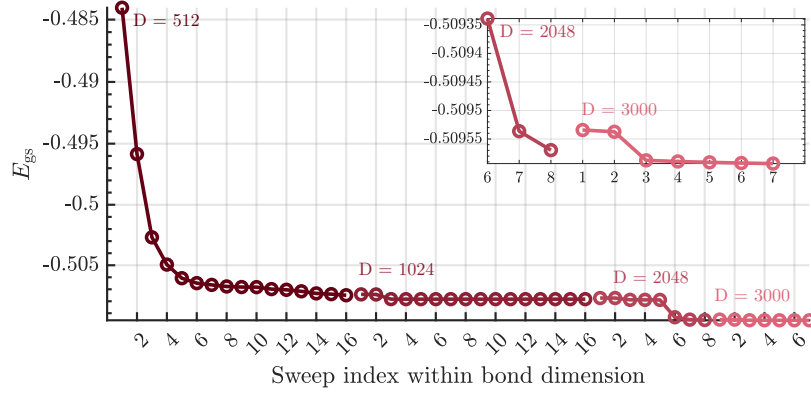


Figure 3.3: DMRG results for a 6×36 triangular lattice in the spin liquid candidate region for $J_2 = 0.125$. The plot shows the evolution of the ground state energy per site after each DMRG sweep for different bond dimensions D . Each segment corresponds to a different bond dimension, with the circles showing the energy after every sweep.

3.3 YC6–0–36 geometry

In the following, we study the ground-state properties of the system for three different coupling regimes, as introduced in section (3.1).

$J_2 = 0$: 120° Néel order

The limit $J_2 = 0$ of the Hamiltonian 2.1 corresponds to the nearest-neighbor Heisenberg model. The ground state for the TLHAF with $J_1 = 1$ has been long established [3, 6, 45] and corresponds to the 120° Néel ordered state, see section (2). This knowledge will be used to benchmark and discuss the outcomes of the different observables we obtain.

To assess the convergence of the DMRG ground-state calculations, we analyze the energy as a function of both the inverse bond dimension $1/D$ and the discarded weight ξ , as shown in Fig. 3.4. The minimal ground state energy per site obtained, with a bond dimension of $D = 3000$ is $E_0 = -0.54852422$ with an associated discarded weight $\xi \sim \mathcal{O}(10^{-7})$. However, for the results presented in this work, we use data obtained with a fixed bond dimension $D = 512$. This yields an energy $E_0 = -0.54835568$, corresponding to a discarded weight $\xi \sim \mathcal{O}(10^{-7})$, and differs from the most accurate energy by approximately 10^{-4} . This choice reflects a compromise between numerical precision and computational efficiency, and we have verified that the observables of interest remain qualitatively robust at this level of approximation.

Following our study we present the results for the equal-time structure factor for this regime. The positions and sharpness of peaks in $\chi_{\mathbf{k}}$ provide insight into the nature of spin correlations in momentum space. Notably, the emergence of sharp Bragg peaks at high-symmetry points in the Brillouin zone is an indication of long-range magnetic order. In figure 3.5 (a), we observe sharp and isolated peaks at \mathbf{K} , \mathbf{K}' and symmetry-equivalent points. Such results are consistent with the expected 120° Néel order on the triangular lattice and

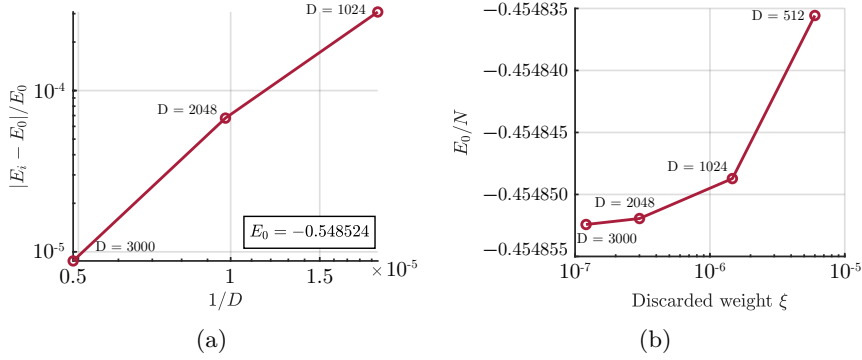


Figure 3.4: DMRG results for a 6×36 triangular lattice in the Néel-ordered regime. Panel (a) shows the convergence of the relative ground state energy per site with respect to the inverse bond dimension $1/D$, while panel (b) shows the dependence of the ground state energy per site on the discarded weight ξ . The inset in panel (a) displays the ground state energy obtained with the largest bond dimension used in our simulations, $D = 3000$.

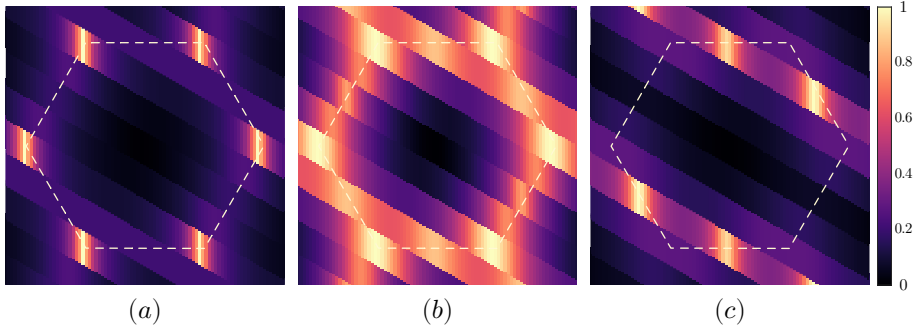


Figure 3.5: Equal-time structure factor $\chi(\mathbf{k})$ for the YC6-0-36 geometry. Panels (a), (b), and (c) correspond to $J_2 = 0$, $J_2 = 0.125$, and $J_2 = 0.2$, respectively. Each plot is normalized independently to its own maximum intensity to highlight the relative distribution of spectral weight across different coupling regimes. The first Brillouin zone is outlined with dashed white lines as a guide to the eye. Panel (a) and (b) are consistent with figure 2 of [17]

confirm the presence of robust long-range magnetic correlations in the ground state [41–43]. We obtained an order parameter $m \sim 0.16$ at the K point, by taking into account the two inner rings on our cylinder. This value is somewhat lower than the widely accepted reported in the literature of $m \sim 0.2$ [8, 41–43]. This discrepancy may stem from finite-size effects or difference in boundary conditions.

In this regime, each spin forms an angle of 120° with its nearest-neighbors (see figure 2.1) leading to a repeating pattern of spin orientations across the lattice. This results in a characteristic three-sublattice spin structure. Such a regular structure gives rise to a stable and spatially coherent pattern in the spin-spin correlations.

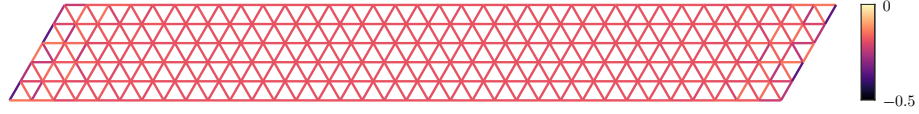


Figure 3.6: Real-space spin-spin correlation function between nearest-neighbouring sites $S_{ij} = \langle \hat{\mathbf{S}}_i \cdot \hat{\mathbf{S}}_j \rangle$, see Eq. (3.4), in the Néel-ordered regime ($J_2 = 0$).

In figure 3.6, we display the nearest-neighbor spin-spin correlations across the system. The strength and sign of the observable $\langle \hat{\mathbf{S}}_i \cdot \hat{\mathbf{S}}_j \rangle$ vary systematically depending on the quantum state. In this case, it can be seen that in the bulk region the correlations are uniformly negative, consistently with antiferromagnetic interactions and the presence of strong magnetic order. This uniformity indicates that the central part of the cylinder remains deep within the magnetically ordered regime. It is important to point out the appearance of some variation in the strength of the correlations near the open edges of the cylinder. Such deviations arise from boundary effects, given by the broken translational symmetry at the edges of the cylinder, which slightly distort the spin configurations in this region.

Figure 3.7 shows the results for the spectral function for the 120° Néel ordered phase using the TaSK algorithm. The data is presented along three high-symmetry paths in the Brillouin zone (see figure 3.2), each cut has been normalized individually.

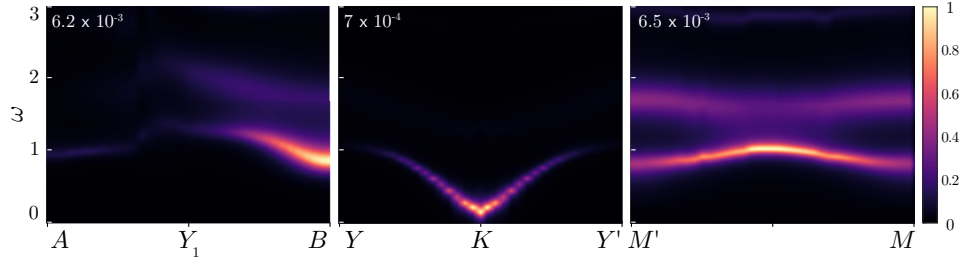


Figure 3.7: Normalized dynamical spin structure factor $S(\mathbf{k}, \omega) / \max S(\mathbf{k}, \omega)$ in the quantum spin liquid candidate phase at $J_2 = 0$, computed on a YC6-0-36 cylinder. The spectral function is shown along three representative cuts in the Brillouin zone, as defined in figure 3.2 (b). Each spectrum is individually normalized to its maximum value to emphasize the relative distribution of spectral weight along each path. As a reference, the normalization factor $1 / \max S(\mathbf{k}, \omega)$ is indicated at the top left of each panel. For comparison, see figure 3, panels (a-c) of [17].

In all three cuts, the dominant feature is a sharp, well-defined excitation at low frequencies, accompanied by a fainter, broader continuum above it. The most prominent low-energy signal appears at the K point, where the mode is soft — i.e., gapless — consistent with the presence of Goldstone magnons in a long-range ordered phase. This result is in excellent agreement with predictions from linear spin wave theory [62], series expansion studies [42, 63], experimental observations via neutron scattering [64], and the results shown in figure 3 (a-b-c)

from Ref. [17].

In contrast, the spectral minima at the M' and M points—located at the midpoints of the Brillouin zone edges—are gapped, which indicates roton-like excitations, in agreement with series expansion and spin wave theory results [42, 63]. We also observe an increase in spectral weight at the midpoing between M' and M , which may result from data broadening induced by CFE.

Furthermore, the quasi-particle ansatz predicts an additional roton minimum at the Y_1 point, located midway between A and B (see figure 3 (a-b-c) from [17]). However, we find no significant spectral weight at this location in our data, suggesting that such an excitation, if present, is either too weak to resolve or not well-defined within our current resolution.

It is important to point out that the data displayed in figure 3.7 has been normalized individually along each momentum path. While this allows for a clearer visualization of dispersion features, it does not accurately reflect their relative spectral weight. From a physical standpoint, such normalization is not meaningful, as it masks the true intensity of excitations across the Brillouin zone. A version of the same data normalized by the global maximum of the full spectrum — preserving the physical strength of features — is provided in Appendix A.

$J_2 = 0.125$: Quantum Spin Liquid Candidate

We now turn to the case of $J_2 = 0.125$, which lies in the expected classical phase boundary between the magnetically ordered 120° Néel phase and the stripe-ordered phase. This region of the phase diagram is characterized for a strong magnetic frustration, that raises between the competition of nearest-neighbor and next-nearest-neighbor interactions in the triangular lattice. This destabilizes the classical long-range order and enhances quantum fluctuations.

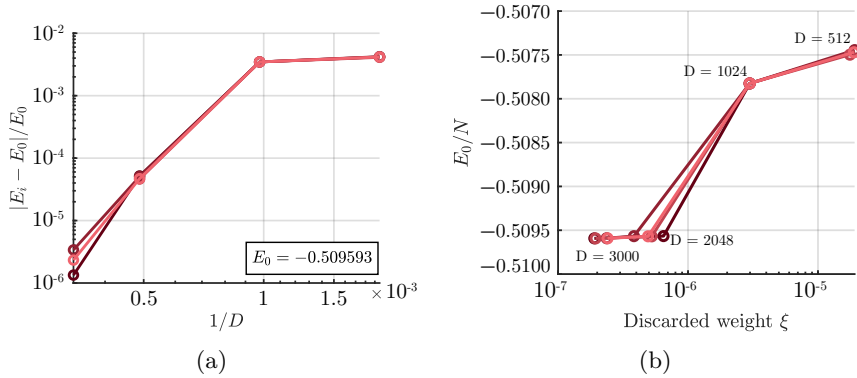


Figure 3.8: DMRG results for a 6×36 triangular lattice in the spin liquid candidate region. Panel (a) shows the convergence of the relative ground state energy per site with respect to the inverse bond dimension $1/D$, while panel (b) displays the dependence of the ground state energy per site on the discarded weight ξ . Each panel includes four different datasets corresponding to independent DMRG runs. The inset in panel (a) displays the ground state energy obtained with the largest bond dimension used in our simulations, $D = 3000$.

To obtain the ground state in the spin-liquid candidate region, we perform four independent CBE-DMRG simulations, each initialized with a different random state. The results are shown in figure B.1, where we show the energy dependence with the inverse of the bond dimension $1/D$ and the discarded weight ξ . These multiple runs help us ensure that the results are representative and not biased by any initial conditions. For the largest bond dimension used, $D = 3000$, the lowest ground-state energy per site obtained is $E_0 = -0.50959308$. The discrepancy between different data sets is at most $10^{-6} - 10^{-7}$, hinting that all converge to the same ground state. As in the $J_2 = 0$ case, we chose to perform our subsequent analysis using data obtained with a fixed bond dimension of $D = 512$ to ensure computational tractability. At this bond dimension, the lowest energy obtained and considered for the future study is $E_0 = -0.50749719$, with a discarded weight of order 10^{-5} . This value only differs with the other CBE-DMRG runs to the order of 10^{-5} , so we can conclude equivalence amongst all data sets. Although the deviation from the best estimate at $D = 3000$ is on the order of 10^{-3} , we ensured that the key observables remain qualitatively stable.

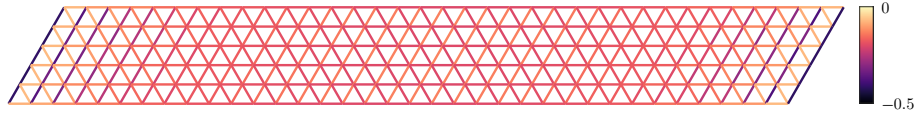


Figure 3.9: Real-space spin-spin correlation function between nearest-neighbouring sites $S_{ij} = \langle \hat{\mathbf{S}}_i \cdot \hat{\mathbf{S}}_j \rangle$, see Eq. (3.4), in the quantum spin liquid candidate ($J_2 = 0.125$).

In figure 3.5(b) we show the equal-time structure factor for this case. While the points K, K' of the Brillouin zone still concentrate slightly higher spectral weight, the peaks are noticeably more diffuse and continuous along the edges of the Brillouin zone. This broadening gives hints of a critical phase without long-range magnetic order [8, 47]. Notably, one can also discern hints of pinch point-like features — narrow, cross-shaped patterns in momentum space — developing at the M points, which further support the interpretation of a quantum spin liquid phase in this intermediate coupling regime. Overall, these observations are consistent with the suppression of Néel order due to frustration and align with previous studies [17, 48].

This behavior is further supported by the nearest-neighbor correlation map shown in figure 3.9. However, compared to the Néel-ordered case at $J_2 = 0$, see figure 3.6, we observe a stronger influence of boundary effects near the open ends of the cylinder. This reflects the more fragile nature of correlations in this regime. Looking closely, one can also see slight hints of symmetry breaking along the spin-chain that arise from the finite size of our system.

Figure 3.10 shows the spectral function along the same regions as shown in figure 3.7, now for the quantum spin liquid candidate regime. Compared to the Néel-ordered case, we observe a downward shift in spectral weight and softening at the M', M and B roton-like points. A low-energy gap opens at the K point, in agreement with [17]. To clarify whether this gap remains in the thermodynamic limit, finite-size scaling of the gap at K would be necessary. That goes beyond the scope of this work.

In a QSL phase, one would expect a spectrum dominated by a broad con-

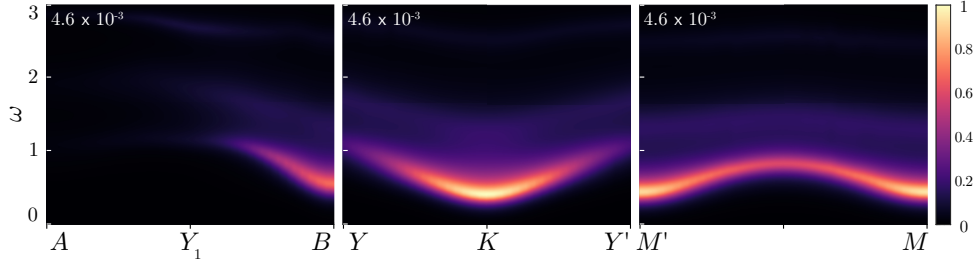


Figure 3.10: Normalized dynamical spin structure factor $S(\mathbf{k}, \omega) / \max S(\mathbf{k}, \omega)$ in the quantum spin liquid candidate phase at $J_2 = 0.125$, computed on a YC6-0-36 cylinder. The spectral function is shown along three representative cuts in the Brillouin zone, as defined in figure 3.2 (b). Each spectrum is individually normalized to its maximum value to emphasize the relative distribution of spectral weight along each path. As a reference, the normalization factor $1 / \max S(\mathbf{k}, \omega)$ is indicated at the top left of each panel. For comparison, see figure 4 of [17].

tinuum of spinon excitations. In our case, the spectrum still shows dominant sharp, low-energy features — particularly at the K , M' and M points. Those momenta correspond to the ordering wave points of the 120° and stripe-ordered phase, respectively. This demonstrates the high frustration in the system: it tries to satisfy simultaneously the J_1 and J_2 interactions, giving rise to a QSL phase [50]. Nevertheless, a broad continuum is also visible above the quasiparticle peaks, especially near the zone boundaries, which is characteristic from the dominated broad spinon-continua of a QSL.

As in the $J_2 = 0$ case, the data in Fig. 3.10 has been normalized individually along each momentum path. A version with a normalization in respect to the global maximum is provided in Appendix A.

$J_2 = 0.2$: Stripe-ordered phase

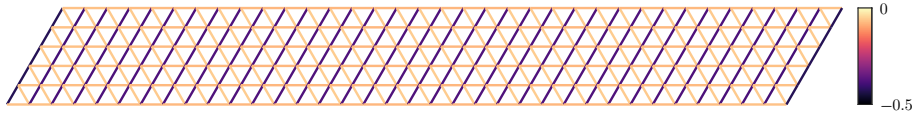


Figure 3.11: Real-space spin-spin correlation function between nearest-neighbouring sites $S_{ij} = \langle \hat{\mathbf{S}}_i \cdot \hat{\mathbf{S}}_j \rangle$, see Eq. (3.4), in the stripe ordered regime ($J_2 = 0.2$).

For completeness, we also examine the case $J_2 = 0.2$, which lies deep in the frustrated regime of the model. In this parameter range, the ground state is known to exhibit stripe order, as previously reviewed in (2), characterized by spins aligning antiferromagnetically along one direction — forming stripes — while exhibiting ferromagnetic alignment between neighboring stripes. This pattern breaks the rotational symmetry of the triangular lattice and reflects a distinct form of magnetic ordering that contrasts sharply with both the 120° Néel order at $J_2 = 0$ and the disordered spin-liquid-like behavior at $J_2 = 0.125$.

The CBE-DMRG results obtained for this state yield a minimal ground-state energy per site of $E_0 = -0.50488522$ at a bond dimension $D = 2048$, with an associated $\xi \sim 10^{-8}$. However, for the observables an MPS of bond dimension $D = 512$, energy per site $E_0 = -0.50487250$ and $\xi \sim 10^{-7}$.

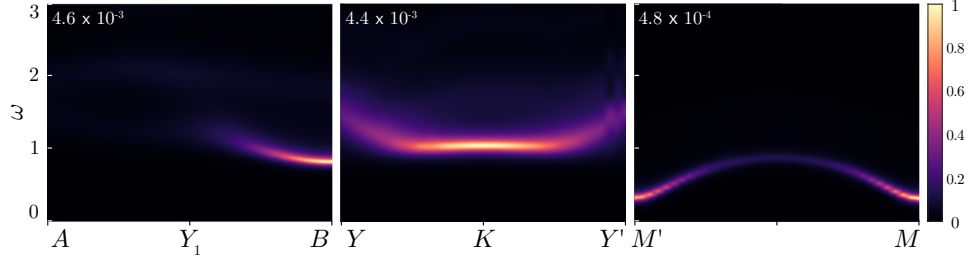


Figure 3.12: Normalized dynamical spin structure factor $S(\mathbf{k}, \omega) / \max S(\mathbf{k}, \omega)$ in the stripe ordered phase at $J_2 = 0.2$, computed on a YC6-0-36 cylinder. The spectral function is shown along three representative cuts in the Brillouin zone, as defined in figure 3.2 (b). Each spectrum is individually normalized to its maximum value to emphasize the relative distribution of spectral weight along each path. As a reference, the normalization factor $1 / \max S(\mathbf{k}, \omega)$ is indicated at the top left of each panel.

In figure 3.5(c) we show the equal-time structure factor for this phase. The emergence of M -point sharp peaks confirm this stripe ordering [47, 65], which breaks rotational symmetry [6]. This ordering also shows in the spin-spin correlations between nearest neighbors, shown in figure 3.11: antiferromagnetically ordered spins exhibit large and negative correlations giving rise to the pattern in the figure. The spectral function for this case show very intense spectral weight at the points M' and M , hinting at a tendency towards the emergence of a gapless Goldstone mode as the value of J_2 increases. Two sharp roton-like minima show at points B and K where the presence of a gap consolidates.

It is worth pointing out that, as the two previous regimes, the data in Fig. 3.12 has been normalized individually along each momentum path. A version of the same data normalized by the global maximum of the full spectrum is provided in Appendix A.

Summary and outlook

Summary. In this thesis, we numerically studied the ground state and dynamical properties of the spin-1/2 J_1 - J_2 Heisenberg antiferromagnet on the triangular lattice. Restricting ourselves to finite-size geometries, specifically the YC6-0-36 cylinder, we employed the CBE-DMRG routine to obtain the approximate ground state solution in the MPS formulation. Once the desired convergence was achieved, we computed static key observables such as the equal-time structure factor and employed the Tangent Space Krylov (TaSK) method to evaluate the dynamical spin structure factor, analyzing the excitation spectrum along three distinct cuts in the Brillouin zone.

First, we benchmarked our results in the well-understood 120° Néel ordered phase at $J_2 = 0$. With a ground state energy of $E_0 = -0.548355$ at bond dimension $D = 512$ and a discarded weight $\xi \sim \mathcal{O}(10^{-7})$, our ground-state-MPS accurately captures the expected phase characteristics. Sharp and isolated peaks appear at the K point for the equal-time structure factor, indicating the robust long-range magnetic correlations compatible. A sharp Goldstone mode can be seen at the same point in the dynamical structure factor, in agreement with previous works [17, 42, 62–64], alongside two roton-like excitations at points M' and M . No significant spectral weight was found in the momentum point Y_1 , for which a roton-like excitation should appear, according to the quasi-particle ansatz [17].

Upon increasing the value of J_2 to the classical phase transition point at $J_2 = 0.125$, a suppression of magnetic order has been observed. We considered a ground-state MPS of energy $E_0 = -0.507497$, bond dimension $D = 512$ and $\xi \sim 10^{-5}$. The broadening of spectral features in equal-time structure factor suggests the loss of long-range magnetic order, also showing hints of pinch-point-like features at the M points. A relaxation of the dynamical structure factor compared to the previous case is observed, with a low-energy-gap opening at the K point. Sharp low-energy features can also be seen at M' , M and B points, however one can see a broad continuum above these quasi-particle peaks. This continuum arises from QSL behavior. No definitive conclusions on the QSL type can be drawn due to finite-size effects, and numerical precision. Further studies for the finite-size scaling of the gap at the K point would be necessary.

Lastly, by setting $J_2 = 0.2$, we enter the so called stripe-phase regime. Very sharp, roton-like minima are observed at points B and K , which are characteristic of this phase. Additionally, we observe indications of a possible

gap closing at point M , and its symmetry-related equivalents, in the ETSF. This is further supported by sharp peaks at these same points in the spectral function.

In comparison to the results of Drescher et al. [17], our TaSK-based study confirms the reliability of the method in capturing the expected spectral features of the triangular lattice Heisenberg model. For the equal-time spin structure factor, we observe broad and diffuse spectral weight that is continuously distributed throughout the Brillouin zone which, compared to Ref. [17], the spectral weight in our results appears slightly more uniformly distributed and smoother in the spin-liquid regime, indicating that TaSK can capture low-energy spin correlations with high consistency. For the dynamical properties, we obtain results that are in strong agreement with those of Ref. [17], further establishing TaSK as a reliable and accurate tool for investigating frustrated quantum magnets. This consistency underscores its potential for future studies, particularly in the directions outlined in the Outlook, where TaSK may prove crucial for exploring larger system sizes and more complex regimes.

Outlook. There are several promising directions in which this work could be extended. One important step would be a more systematic finite-size scaling analysis of the spectral gap at the K point, which could help determine whether the quantum spin liquid candidate phase is truly gapless or possesses a small but finite spin gap — thus offering deeper insight into the nature of this exotic phase.

Another key direction involves studying a Gutzwiller-projected fermionic wavefunction representing a $U(1)$ Dirac spin liquid. We plan to compute the corresponding spectral functions using the TaSK algorithm applied to this ansatz, and also use it as an initial state for DMRG, enabling the algorithm to optimize the state before applying TaSK again. This approach could provide a bridge between variational and unbiased methods.

Additionally, the exploration of alternative geometries such as the $YC6-2-L_y$ cylinder — where the allowed momenta intersect the Dirac points — remains an intriguing path forward. Although our initial data in this geometry has been inconclusive, see Appendix B, further targeted studies could reveal more information about the system's behavior and potentially expose new features of the spin liquid phase.

Complementary Plots for the YC6–0–36 geometry

In the main text, we present the dynamical spin structure factor $S(\mathbf{k}, \omega)$ normalized individually for each momentum cut in the Brillouin zone. While this emphasizes the relative distribution of spectral weight within each cut, it obscures how the weight is shared across different regions of momentum space. To provide a more physically meaningful comparison, figure B.2 shows the spectral function normalized per full spectrum, i.e., by the maximum over all three momentum cuts. This allows for a direct comparison of how the spectral weight is distributed across symmetry points.

As expected, in the ordered phase at $J_2 = 0$, the Goldstone mode at the K -point dominates the spectral response, carrying most of the total weight. Similarly, for $J_2 = 0.2$, which lies deep in the stripe-ordered phase, the low-energy roton modes at the M -points are prominent and account for most of the spectral weight. In contrast, in the intermediate spin-liquid phase near $J_2 = 0.125$, the spectral weight is more evenly distributed across all symmetry points, indicating the absence of dominant long-range order.

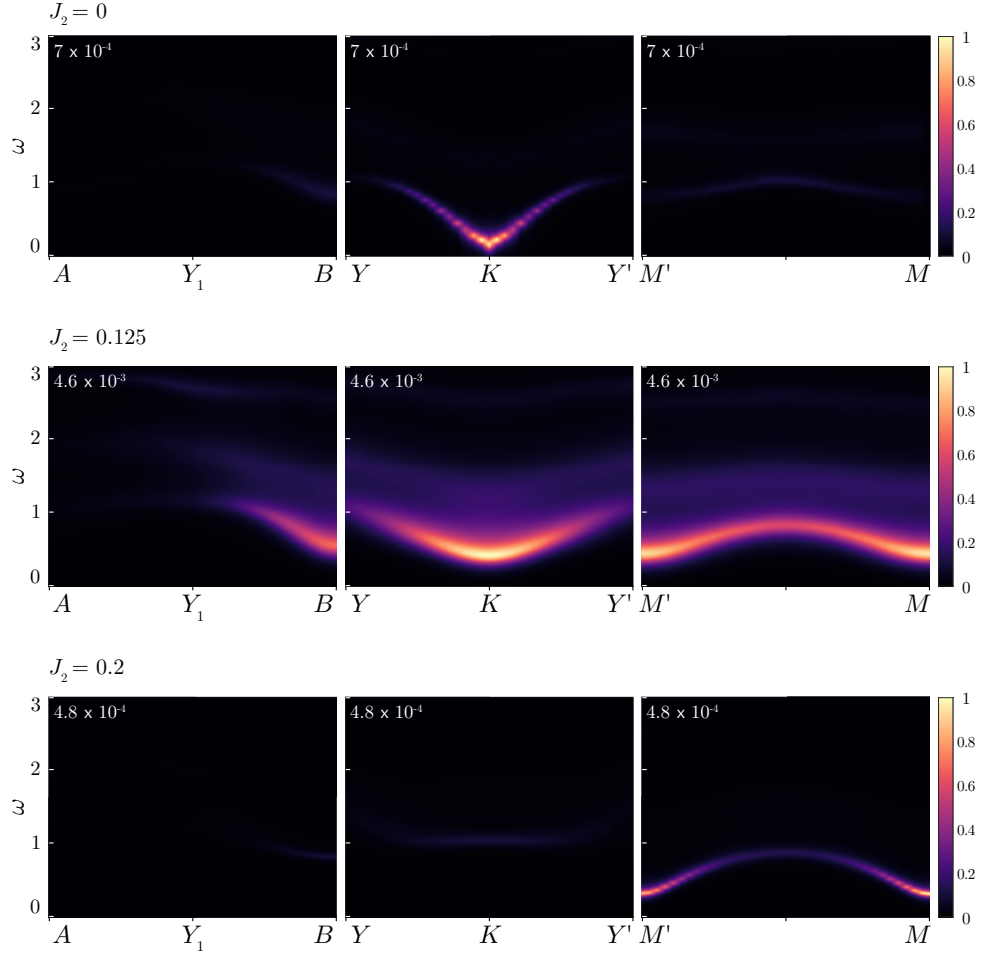


Figure A.1: Normalized dynamical spin structure factor $S(\mathbf{k}, \omega) / \max S(\mathbf{k}, \omega)$ for $J_2 = 0$, $J_2 = 0.125$ and $J_2 = 0.125$, computed on a YC6-0-36 cylinder. The spectral function is shown along three representative cuts in the Brillouin zone, as defined in figure 3.2. The spectrum for each J_2 value is normalized taking the maximum value along the three cuts. As a reference, the normalization factor $1 / \max S(\mathbf{k}, \omega)$ is indicated at the top left of each panel.

YC6-2-36 geometry

To investigate whether the Dirac cone structure of a potential U(1) Dirac spin liquid leaves any observable imprint in the dynamical spin structure factor, we examined the YC6-2-36 geometry. This geometry is of particular interest because its set of allowed momenta intersects the Dirac points located at $\pm \mathbf{Q} = \pm \left(\frac{\pi}{2}, \frac{\pi}{2\sqrt{3}} \right)$.

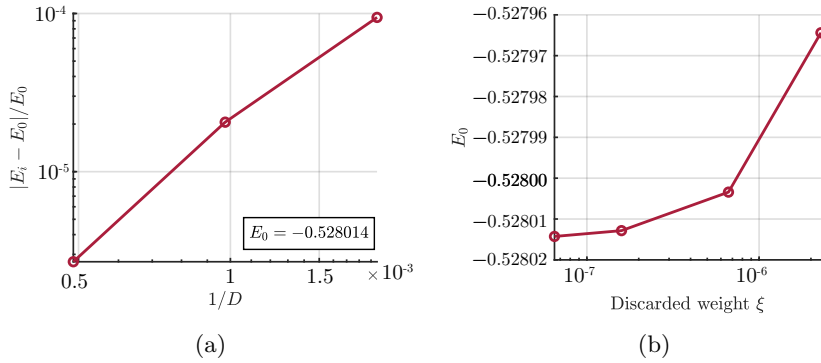


Figure B.1: DMRG results for a 6×36 triangular lattice in the spin liquid candidate region for the YC6-2-36 geometry. Panel (a) shows the convergence of the relative ground state energy per site with respect to the inverse bond dimension $1/D$, while panel (b) displays the dependence of the ground state energy per site on the discarded weight ξ . Each panel includes four different datasets corresponding to independent DMRG runs. The inset in panel (a) displays the ground state energy obtained with the largest bond dimension used in our simulations, $D = 3000$.

We present both the ground state results and the corresponding dynamical spectra through the cut shown in figure 3.2(d) obtained. As anticipated, no pronounced features are observed at the Dirac points in the dynamical data. This is consistent with theoretical expectations: the dynamical spin structure factor $S(\mathbf{k}, \omega)$ probes spin-1 excitations, whereas the Dirac cones correspond to gapless spin-1/2 spinons. Since the spin operator does not couple directly to individual spinons, but rather to two-spinon excitations, and the spinon density of states vanishes linearly at the Dirac point, the resulting spectral

weight remains broad and suppressed in that region of momentum space.

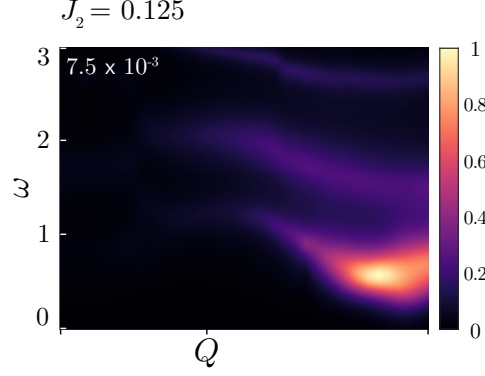


Figure B.2: Normalized dynamical spin structure factor $S(\mathbf{k}, \omega) / \max S(\mathbf{k}, \omega)$ for $J_2 = 0$, $J_2 = 0.125$, and $J_2 = 0.2$, computed on a YC6–0–36 cylinder. The spectral function is shown along the momentum cut defined in figure 3.2(d). For each J_2 , the spectrum is normalized by the maximum value across the three cuts. The corresponding normalization factor $1 / \max S(\mathbf{k}, \omega)$ is indicated at the top left of each panel.

Bibliography

- [1] L. Savary and L. Balents, “Quantum spin liquids: a review”, [Reports on Progress in Physics](#) **80**, 016502 (2017).
- [2] D. A. Huse and V. Elser, “Simple Variational Wave Functions for Two-Dimensional Heisenberg Spin- $\frac{1}{2}$ Antiferromagnets”, [Physical Review Letters](#) **60**, 2531 (1988).
- [3] Th. Jolicoeur, E. Dagotto, E. Gagliano, and S. Bacci, “Ground-state properties of the $S=1/2$ Heisenberg antiferromagnet on a triangular lattice”, [Physical Review B](#) **42**, 4800 (1990).
- [4] T. Momoi, “Low-lying excited states of quantum antiferromagnets on a triangular lattice”, [Journal of Statistical Physics](#) **75**, 707 (1994).
- [5] Th. Jolicoeur, E. Dagotto, E. Gagliano, and S. Bacci, “Ground-state properties of the $S = 1/2$ Heisenberg antiferromagnet on a triangular lattice”, [Physical Review B](#) **42**, 4800 (1990).
- [6] Y. Iqbal, W.-J. Hu, R. Thomale, D. Poilblanc, and F. Becca, “Spin liquid nature in the Heisenberg J_1 - J_2 triangular antiferromagnet”, [Physical Review B](#) **93** (2016).
- [7] W.-J. Hu, S.-S. Gong, W. Zhu, and D. N. Sheng, “Competing Spin Liquid States in the Spin- $1/2$ Heisenberg Model On Triangular Lattice”, [Physical Review B](#) **92** (2015).
- [8] Z. Zhu and S. R. White, “Spin liquid phase of the $S=1/2$ J_1 - J_2 Heisenberg model on the triangular lattice”, [Physical Review B](#) **92** (2015).
- [9] Y. Shimizu, K. Miyagawa, K. Kanoda, M. Maesato, and G. Saito, “Spin Liquid State in an Organic Mott Insulator with a Triangular Lattice”, **91** (2003).
- [10] Y. Li, S. Bachus, B. Liu, I. Radelytskyi, A. Bertin, A. Schneidewind, Y. Tokiwa, A. A. Tsirlin, and P. Gegenwart, “Rearrangement of uncorrelated valence bonds evidenced by low-energy spin excitations in YbMgGaO_4 ”, [Physical Review Letters](#) **122** (2019).
- [11] N. Li, M. T. Xie, Q. Huang, Z. W. Zhuo, Z. Zhang, E. S. Choi, Y. Y. Wang, H. Liang, Y. Sun, D. D. Wu, Q. J. Li, H. D. Zhou, G. Chen, X. Zhao, Q. M. Zhang, and X. F. Sun, “Thermodynamics and heat transport of quantum spin liquid candidates NaYbS_2 and NaYbSe_2 ”, [Physical Review B](#) **110** (2024).

- [12] Y. Oshima, Y. Ishii, F. L. Pratt, I. Watanabe, H. Seo, T. Tsumuraya, T. Miyazaki, and R. Kato, “Quasi-One-Dimensional Spin Dynamics in a Molecular Spin Liquid System”, *Physical Review Letters* **133** (2024).
- [13] W. Zhang, J. Cao, L. Wang, Z. Xia, Z. Wang, J. Zhao, Z. Fu, and Z. Ouyang, “A method of detecting magnetic interaction in the quantum spin liquid material NaYbSe₂ through magnetic dilution”, *Journal of Applied Physics* **137** (2025).
- [14] A. Wietek and A. M. Läuchli, “Sublattice coding algorithm and distributed memory parallelization for large-scale exact diagonalizations of quantum many-body systems”, *Physical Review E* **98**, 033309 (2018).
- [15] P. Henelius and A. W. Sandvik, “Sign problem in Monte Carlo simulations of frustrated quantum spin systems”, *Physical Review B* **62**, 1102 (2000).
- [16] O. Kovalska, A. Gleis, and J. Von Delft, “In preparation”,
- [17] M. Drescher, L. Vanderstraeten, R. Moessner, and F. Pollmann, “Dynamical Signatures of Symmetry Broken and Liquid Phases in an $S=1/2$ Heisenberg Antiferromagnet on the Triangular Lattice”, *Physical Review B* **108** (2023).
- [18] A. Wietek, L. Staszewski, M. Ulaga, P. L. Ebert, H. Karlsson, S. Sarkar, H. Shackleton, A. Sinha, and R. D. Soares, *XDiag: Exact Diagonalization for Quantum Many-Body Systems*, (May 26, 2025) [arXiv:2505.02901 \[cond-mat\]](https://arxiv.org/abs/2505.02901), <http://arxiv.org/abs/2505.02901> (visited on 07/16/2025), pre-published.
- [19] M. C. Bañuls, “Tensor Network Algorithms: a Route Map”, *Annual Review of Condensed Matter Physics* **14**, 173 (2023).
- [20] M. B. Hastings, “An Area Law for One Dimensional Quantum Systems”, *Journal of Statistical Mechanics: Theory and Experiment* **2007**, P08024 (2007).
- [21] J. I. Cirac, D. Pérez-García, N. Schuch, and F. Verstraete, “Matrix product states and projected entangled pair states: Concepts, symmetries, theorems”, *Reviews of Modern Physics* **93** (2021).
- [22] A. Gleis, J.-W. Li, and J. Von Delft, “Projector formalism for kept and discarded spaces of matrix product states”, *Physical Review B* **106** (2022).
- [23] S. R. White, “Density matrix formulation for quantum renormalization groups”, *Physical Review Letters* **69**, 2863 (1992).
- [24] S. R. White, “Density-matrix algorithms for quantum renormalization groups”, *Physical Review B* **48**, 10345 (1993).
- [25] S. Östlund and S. Rommer, “Thermodynamic Limit of Density Matrix Renormalization”, *Physical Review Letters* **75**, 3537 (1995).
- [26] G. Vidal, “Efficient classical simulation of slightly entangled quantum computations”, *Physical Review Letters* **91** (2003).
- [27] F. Verstraete and J. I. Cirac, *Renormalization algorithms for Quantum-Many Body Systems in two and higher dimensions*, (July 2, 2004) [arXiv:cond-mat/0407066](https://arxiv.org/abs/cond-mat/0407066), <http://arxiv.org/abs/cond-mat/0407066> (visited on 07/25/2025), pre-published.

- [28] G. Vidal, “Efficient simulation of one-dimensional quantum many-body systems”, *Physical Review Letters* **93** (2004).
- [29] U. Schollwöck, “The density-matrix renormalization group”, *Rev. Mod. Phys.* **77** (2005).
- [30] E. Pavarini, E. Koch, D. Vollhardt, A. I. Lichtenstein, Institute for Advanced Simulation, German Research School for Simulation Sciences, and Deutsche Forschungsgemeinschaft, eds., *The LDA+DMFT approach to strongly correlated materials: lecture notes of the Autumn School 2011 Hands-on LDA+DMFT: at Forschungszentrum Jülich, 4-7 October 2011*, Schriften Des Forschungszentrums Jülich. Reihe Modeling and Simulation Band 1 (Forschungszentrum Jülich, Zentralbibliothek, Verl, Jülich, 2011), 436 pp.
- [31] A. Gleis, J.-W. Li, and J. Von Delft, “Controlled Bond Expansion for Density Matrix Renormalization Group Ground State Search at Single-Site Costs”, *Physical Review Letters* **130** (2023).
- [32] S. R. White, “Density matrix renormalization group algorithms with a single center site”, *Physical Review B* **72**, 180403 (2005).
- [33] E. M. Stoudenmire and S. R. White, “Studying Two Dimensional Systems With the Density Matrix Renormalization Group”, *Annual Review of Condensed Matter Physics* **3**, 111 (2012).
- [34] A. Gleis, J.-W. Li, and J. von Delft, *Reply to comment on "Controlled bond expansion for Density Matrix Renormalization Group ground state search at single-site costs"*, (Jan. 21, 2025) [arXiv:2501.12291 \[cond-mat\]](https://arxiv.org/abs/2501.12291), <http://arxiv.org/abs/2501.12291> (visited on 07/30/2025), pre-published.
- [35] J. Haegeman, B. Pirvu, D. J. Weir, J. I. Cirac, T. J. Osborne, H. Verschelde, and F. Verstraete, “Variational matrix product ansatz for dispersion relations”, *Physical Review B* **85**, 100408 (2012).
- [36] J. Haegeman, S. Michalakis, B. Nachtergaele, T. J. Osborne, N. Schuch, and F. Verstraete, “Elementary Excitations in Gapped Quantum Spin Systems”, *Physical Review Letters* **111**, 080401 (2013).
- [37] J. Haegeman, T. J. Osborne, and F. Verstraete, “Post-matrix product state methods: To tangent space and beyond”, *Physical Review B* **88**, 075133 (2013).
- [38] L. Vanderstraeten, J. Haegeman, and F. Verstraete, “Tangent-space methods for uniform matrix product states”, *SciPost Physics Lecture Notes*, **7** (2019).
- [39] W.-L. Tu, H.-K. Wu, N. Schuch, N. Kawashima, and J.-Y. Chen, “Generating function for tensor network diagrammatic summation”, *Physical Review B* **103**, 205155 (2021).
- [40] M. Van Damme, R. Vanhove, J. Haegeman, F. Verstraete, and L. Vanderstraeten, “Efficient matrix product state methods for extracting spectral information on rings and cylinders”, *Physical Review B* **104**, 115142 (2021).
- [41] L. Capriotti, A. E. Trumper, and S. Sorella, “Long-Range Néel Order in the Triangular Heisenberg Model”, *Physical Review Letters* **82**, 3899 (1999).

- [42] W. Zheng, J. O. Fjærestad, R. R. P. Singh, R. H. McKenzie, and R. Coldea, “Excitation spectra of the spin-12triangular-lattice Heisenberg antiferromagnet”, *Physical Review B* **74** (2006).
- [43] S. R. White and A. L. Chernyshev, “Neél Order in Square and Triangular Lattice Heisenberg Models”, *Physical Review Letters* **99** (2007).
- [44] Y. Zhou, K. Kanoda, and T.-K. Ng, “Quantum spin liquid states”, *Reviews of Modern Physics* **89** (2017).
- [45] J. Willsher and J. Knolle, *Dynamics and stability of $U(1)$ spin liquids beyond mean-field theory*, (Mar. 18, 2025) [arXiv:2503.13831 \[cond-mat\]](https://arxiv.org/abs/2503.13831), <http://arxiv.org/abs/2503.13831> (visited on 07/12/2025), pre-published.
- [46] J. Oitmaa, “Magnetic phases in the J1-J2 Heisenberg antiferromagnet on the triangular lattice”, *Physical Review B* **101** (2020).
- [47] R. Kaneko, S. Morita, and M. Imada, “Gapless Spin-Liquid Phase in an Extended Spin 1/2 Triangular Heisenberg Model”, *Journal of the Physical Society of Japan* **83**, 093707 (2014).
- [48] F. Ferrari and F. Becca, “Dynamical structure factor of the J_1 - J_2 Heisenberg model on the triangular lattice: magnons, spinons, and gauge fields”, *Physical Review X* **9** (2019).
- [49] S. Hu, W. Zhu, S. Eggert, and Y.-C. He, “Dirac Spin Liquid on the Spin-1/2 Triangular Heisenberg Antiferromagnet”, *Physical Review Letters* **123** (2019).
- [50] N. E. Sherman, M. Dupont, and J. E. Moore, “Spectral function of the J1-J2 Heisenberg model on the triangular lattice”, *Physical Review B* **107** (2023).
- [51] P. Anderson, “Resonating valence bonds: A new kind of insulator?”, **8**, 153.
- [52] X.-G. Wen, “Zoo of quantum-topological phases of matter”, *Reviews of Modern Physics* **89** (2017).
- [53] J. Knolle and R. Moessner, “A Field Guide to Spin Liquids”, *Annual Review of Condensed Matter Physics* **10**, 451 (2019).
- [54] G. Zheng, Y. Zhu, K.-W. Chen, B. Kang, D. Zhang, K. Jenkins, A. Chan, Z. Zeng, A. Xu, O. A. Valenzuela, J. Blawat, J. Singleton, P. A. Lee, S. Li, and L. Li, “Unconventional Magnetic Oscillations in Kagome Mott Insulators”, *Proceedings of the National Academy of Sciences* **122** (2025).
- [55] L. Venema, B. Verberck, I. Georgescu, G. Prando, E. Couderc, S. Milana, M. Maragkou, L. Persechini, G. Pacchioni, and L. Fleet, “The quasiparticle zoo”, *Nature Physics* **12**, 1085 (2016).
- [56] A. O. Scheie, M. Lee, K. Wang, P. Laurell, E. S. Choi, D. Pajerowski, Q. Zhang, J. Ma, H. D. Zhou, S. Lee, S. M. Thomas, M. O. Ajeesh, P. F. S. Rosa, A. Chen, V. S. Zapf, M. Heyl, C. D. Batista, E. Dagotto, J. E. Moore, and D. A. Tennant, *Spectrum and low-energy gap in triangular quantum spin liquid NaYbSe_2* , (June 25, 2024) [arXiv:2406.17773 \[cond-mat\]](https://arxiv.org/abs/2406.17773), <http://arxiv.org/abs/2406.17773> (visited on 07/13/2025), pre-published.

- [57] A. Szasz, J. Motruk, M. P. Zaletel, and J. E. Moore, “Chiral Spin Liquid Phase of the Triangular Lattice Hubbard Model: A Density Matrix Renormalization Group Study”, [Physical Review X](#) **10** (2020).
- [58] A. Weichselbaum, “Non-abelian symmetries in tensor networks: a quantum symmetry space approach”, [Annals of Physics](#) **327**, 2972 (2012).
- [59] A. Weichselbaum, “X-Symbols for Non-Abelian Symmetries in Tensor Networks”, [Physical Review Research](#) **2** (2020).
- [60] A. Weichselbaum, “QSpace - An open-source tensor library for Abelian and non-Abelian symmetries”, [SciPost Physics Codebases](#), 40 (2024).
- [61] A. Gleis and J.-W. Li, “Supplemental material: Controlled bond expansion for DMRG ground state search at single-site costs”,
- [62] A. V. Chubukov, S. Sachdev, and J. Ye, “Theory of two-dimensional quantum Heisenberg antiferromagnets with a nearly critical ground state”, [Physical Review B](#) **49**, 11919 (1994).
- [63] W. Zheng, J. O. Fjaerestad, R. R. P. Singh, R. H. McKenzie, and R. Coldea, “Anomalous Excitation Spectra of Frustrated Quantum Antiferromagnets”, [Physical Review Letters](#) **96** (2006).
- [64] J. Ma, Y. Kamiya, T. Hong, H. B. Cao, G. Ehlers, W. Tian, C. D. Batista, Z. L. Dun, H. D. Zhou, and M. Matsuda, “Static and Dynamical Properties of the Spin-1/2Equilateral Triangular-Lattice AntiferromagnetBa3CoSb2O9”, [Physical Review Letters](#) **116** (2016).
- [65] C. A. Gallegos, S. Jiang, S. R. White, and A. L. Chernyshev, “Phase Diagram of the Easy-Axis Triangular-Lattice J_1 - J_2 Model”, [Physical Review Letters](#) **134** (2025).